A THEORETICAL STUDY ON ALKALI SEEDING OF ARCJET THRUSTERS

by

Folusho Taiwo Oyerokun

M.S., Kiev Institute of Civil Aviation Engineers, Kiev, Ukraine 1993

SUBMITTED TO THE DEPARTMENT OF AERONAUTICS AND ASTRONAUTICS
IN PARTIAL FULFILLMENT OF THE REQUIREMENTS FOR THE DEGREE OF

Master of Science

in Aeronautics and Astronautics

at the

Massachusetts Institute of Technology

September 1997

Signature of Author _____

Department of Aeronautics and Astronautics

July 3, 1997

Certified by _____

Professor Manuel Martinez-Sanchez, Thesis Supervisor

Department of Aeronautics and Astronautics

Accepted by _____

Professor Jaime Peraire

Chairman, Department Graduate Committee

A Theoretical Study on Alkali Seeding of Arcjet Thrusters

by

Folusho Taiwo Oyerokun

Submitted to the Department of Aeronautics and Astronautics
on July 3, 1997, in partial fulfillment of the requirements for the degree of
Master of Science in Aeronautics and Astronautics

Abstract

A model has been developed to assess the feasibility of reducing the frozen losses in a hydrogen arcjet by adding very small amounts of easily ionizable cesium vapor. It is found that within reasonable constraints on the constrictor geometry, and without allowing the electron temperature to exceed about $7000K$, both the ionization and the hydrogen dissociation losses can essentially be eliminated, and a specific impulse of about 850 seconds can be obtained.

A small perturbation analysis was performed on the nonequilibrium governing equations with the intention of probing the physics of ionization instabilities that occur in both the cesium and hydrogen ionization ranges. The results from this analysis show that the seed ionization instability occurs at electron temperatures where Coulomb interactions are important. Its occurence in the system was found to result in driving the electron temperature above its threshold value for near-full ionization of the seed. The hydrogen ionization instability was found to occur when the ratio of electrons from hydrogen to the total present is about 2%.

Thesis Supervisor: Manuel Martinez-Sanchez
Title: Professor

Acknowledgement

I am very grateful to my thesis supervisor, Professor Manuel Martinez-Sanchez, for his guidance throughout the course of this work. His insight, patience, support and encouragement were essential to the successful completion of this research. He is an example of the fact that humility and brilliance are not mutually exclusive.

I also would like to recognize Dr. David Gonzales for his advice and friendship. His input to this project, as well as to my life, are invaluable.

I am so appreciative to the Aeronautics and Astronautics department for offering me such a wonderful opportunity to study in their department. I would also like to acknowledge the Zacharchenko Foundation and the Air Force Office of Scientific Research for providing the funding for this research.

I am indebted to my colleagues in both the Space Systems and Fluid Dynamics Research Laboratories whose camaraderie greatly eased the pressure generally associated with graduate study at MIT. My sincere thanks, especially, go to Ray, Guy, Greame, Mike, Ed and Tolu.

I want to express my gratitudes to the many friends who stood with me during my stay at MIT: roommates, the MIT Christian Community as a whole, Maranatha Christian Fellowship and Tree of Life City Church. I especially thank Wole, Joel, Araz, Kamel, Durodemi, Abraham and Chris for being examples of friends that stick closer than brothers.

I want thank my parents for their selfless love and support. Their sacrifice to ensure that I obtain my dream is greatly appreciated. This thesis is dedicated to them.

Finally, I give thanks to my Heavenly Father for His provision, faithfulness, blessings, love and abundance grace toward me, the Holy Spirit for being a wonderful Paraklete and my Lord and Savior, Jesus Christ, for giving me a new life, peace, joy and hope through His work of atonement.

Blessed is the man who trusts in the LORD,

And whose hope is the LORD.

For he shall be like a tree planted by the waters,

Which spreads out its roots by the river,

And will not fear when heat comes;

But its leaf will be green,

And will not be anxious in the year of drought,

Nor will cease from yielding fruit.

- Jeremiah 17:7-8, New King James Version.

Contents

1 Introduction **13**

1.1 Electrothermal Arcjets 13

1.2 Frozen Losses 14

1.3 Alkali Seeding of Arcjets 16

1.4 Thesis Overview 16

2 Governing Equations **19**

2.1 Thermal Properties 19

2.2 Transport Properties 21

2.3 Flow Chemistry 25

2.3.1 Dissociation 25

2.3.2 Ionization 27

2.4 Continuity Equations 27

2.5 Momentum Equations 28

2.6 Energy Equations 30

2.7 Electric Potential Equation 30

3 A Simplified Flow Analysis **33**

3.1 Ionizational and Dissociative Equilibrium 33

3.2 Steady Flow Equations 34

3.3 Method of Solution 38

3.3.1 Initial and Boundary Conditions 38

3.3.2 Procedure 39

3.3.3 Performance 40

3.4 Discussion of Results 41

3.5 Summary and Conclusions 43

4 Stability Analysis **53**

4.1 Governing Equations 53

4.2 Linearization of the Governing Equations 54

4.3 Dispersion Relations 59

4.4 Results 63

4.4.1 Stability Behavior as a Function of Electron Temperature 65

4.4.2 Stability Behavior as a Function of Gas Temperature and Pressure . 66

4.4.3 Stability Behavior as a Function of Cesium Seed Fraction 66

4.5 Summary and Conclusions 67

5 Conclusions **75**

5.1 Achievements 75

5.2 Recommendation for Future Work 76

A Tables of Hydrogen Collision Cross Sections and Integrals **77**

List of Figures

1-1 Schematic Diagram of an Arcjet Thruster 14

1-2 Theoretical variation of frozen flow efficiency with specific impulse for hydrogen at various pressures. 15

1-3 Conductivity of hydrogen, seeded with 0.1% cesium per mole 17

2-1 Electron-Cesium momentum transfer collision cross section 24

2-2 Reaction Rate Coefficient for $e - H_2$ Dissociating Collisions 26

2-3 Inelastic collision correction factor for some polyatomic species 31

3-1 Physical domain 39

3-2 Exit electron temperature, L/D and frozen losses vs. seed fraction 44

3-3 Specific impulse and arc voltage vs. seed fraction 45

3-4 Exit electron temperature, L/D and frozen losses vs. total pressure 45

3-5 Specific impulse and arc voltage vs. total pressure 46

3-6 Exit electron temperature, L/D and frozen losses vs. current 46

3-7 Specific impulse and arc voltage vs. current 47

3-8 Specific impulse and arc voltage vs. inlet Mach number 47

3-9 Exit electron temperature, L/D and frozen losses vs. inlet Mach number . . 48

3-10 Gas velocity contour plot 49

3-11 Gas temperature contour plot 50

3-12 Electron temperature contour plot 51

4-1 Nondimensional Imaginary Frequency versus wave vector 64

4-2 Imaginary frequency vs electron temperature 68

4-3 Relative perturbation in conductivity versus electron temperature 69

4-4 Electron density perturbation and nondimensional parameter C versus electron temperature 70
4-5 Atomic hydrogen density perturbation versus electron temperature 71
4-6 Threshold values of electron temperature versus gas temperature at different pressures 72
4-7 Threshold values of electron temperature versus cesium seed fraction 73

List of Tables

1.1 Performance of typical arcjet thrusters 14

2.1 Values of $ln\Lambda$ 23

3.1 Typical Results 41

4.1 Approximate values of electron temperature below which seed ionization instability occurs for a given seed fraction 67

A.1 Average Electron Collision Cross-Sections 77

A.2 Average Effective Collision Integrals 78

Chapter 1

Introduction

1.1 Electrothermal Arcjets

Arcjets belong to the class of electric propulsion devices known as electrothermal thrusters. In electrothermal thrusters, the propellant is heated electrically and then expanded in a nozzle, where its thermal energy is converted directly into kinetic, thereby creating thrust. The other member of this class is the resistojet. An arcjet differs from a resistojet in the way heat is supplied to the working gas: in an arcjet, the propellant is heated through direct contact with an electric discharge, while in a resistojet, the propellant is heated through forced convective contact with electrically heated solid surfaces (coils, walls et cetera). The performance characteristics of typical arcjets thrusters are displayed in Table 1.1 [17]. Arcjets, because of their high specific impulses at relatively low thrusts, are suitable for space missions such as orbit transfer and station keeping of communication satellites.

The schematic diagram of a typical arcjet thruster is shown in Fig. 1-1. The thruster consists of a cathode, a cylindrical rod with a conical tip; an arc chamber (or constrictor) and nozzle. The constrictor and the nozzle together make up the anode. The electrodes are normally made from tungsten (melting point $3680K$), and are separated by a high temperature dielectric, such as boron nitride. The role of the constrictor is to stabilize the arc in a fixed, central position. Another method used in maintaining arc stability, is by injecting the propellant with a swirl into the chamber. The central portion of the gas (about 1 mm in thickness) is heated to very high temperatures through collisions with high energy arc electrons, ionizes and then mixes with the cooler outer region. Expansion of the gas is then carried out in a high expansion ratio nozzle . A direct result of the

Table 1.1: Performance of typical arcjet thrusters

Input Power, KW	1	30	30	30	30 AC	200
Propellant	H_2	H_2	H_2	NH_3	H_2	H_2
Thrust, Newtons	0.044	3.35	1.77	2.37	2.26	6.80
Specific Impulse, sec	1100	1010	1520	1012	1020	2120
Thrust efficiency	0.35	0.54	0.44	0.39	0.38	0.35

mixing is the presence of a nonuniform temperature distribution, with temperatures ranging from $30,000K$ in the core of the constrictor to between $1000 - 2500K$ at the walls, hence protecting the walls. The thruster walls are cooled regeneratively or through radiative transfer to outer space. A light gas such as hydrogen or its compounds (e.g. hydrazine or ammonia) is normally used as propellant to obtain a high specific impulse for a given temperature. In addition to being light, they are also good coolants because of their high specific heat capacity.

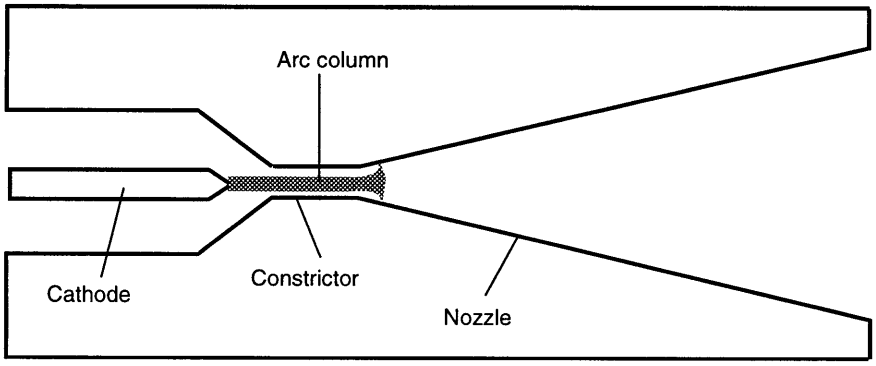

Figure 1-1: Schematic Diagram of an Arcjet Thruster

1.2 Frozen Losses

At very high temperatures, typical of the gas in an arcjet constrictor, substantial dissociation of molecular hydrogen and ionization of atomic hydrogen (in the core) occur. However, due to the very fast expansion that takes place in the nozzle, the species are unable to relax to their equilibrium values, so that a fraction of the energy, that otherwise would have been converted to kinetic, is tied up in ionization and dissociation modes. Losses of this type are

referred to as frozen flow losses. The magnitude of these losses is seen in the modeling work of Miller [10] on a radiation-cooled hydrogen arcjet operating at $.1\,g/sec$ flow rate, $1.2\,atm$ chamber pressure, $100\,A$ current and $11.5\,kw$ power. The work shows that 17.5% of the exit plane energy flux is in the form of ionization energy, and 30% in the form of dissociation energy. Including thermal energy, this is leaves only 39% for the flow kinetic energy.

A mitigating strategy that has been employed is to operate the device at high pressure, so as to lower the chamber dissociation level and increase the recombination rate in the nozzle[5]. A useful performance index in characterizing the effect of frozen flow on nozzle performance is the frozen flow efficiency, defined as the ratio of enthalpy converted to jet kinetic energy to that imparted in the chamber assuming no recombination in the nozzle,

$$\eta_f = \frac{h_c - h_e}{h_c},$$

where h_c and h_e are the chamber and nozzle exit enthalpies respectively. Figure 1-2 shows the effect of pressure on frozen flow efficiency calculated using a very simplified one dimensional model [7]. The disadvantages of operating at high pressures are increased stress on the hot chamber walls and erosion of the nozzle throat; also the requirement of smaller orifices, leading to higher arc temperature and consequently to increase in arc radiation losses.

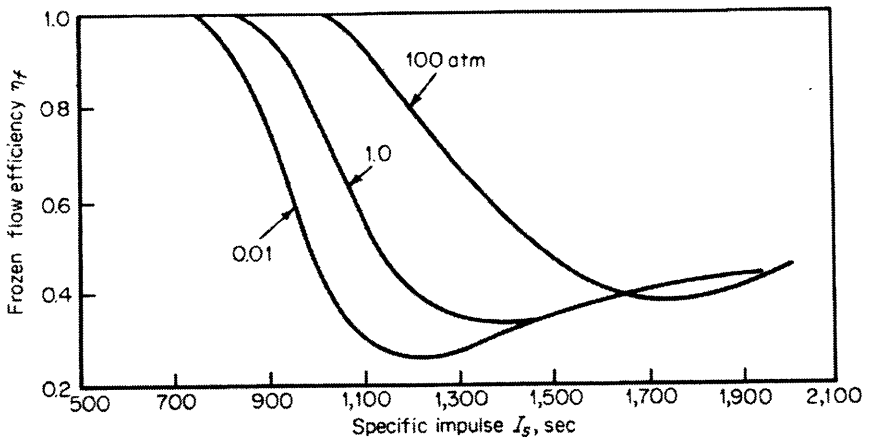

Figure 1-2: Theoretical variation of frozen flow efficiency with specific impulse for hydrogen at various pressures.

1.3 Alkali Seeding of Arcjets

A standard procedure used in MHD power conversion technology in obtaining good electrical conductivity without ionizing the working gas is through the introduction of an easily ionizable alkali seed (vapor) into the propellant stream[14]. The presence of small fractions of the seed ions establishes a conductive path between the electrodes at temperatures below ionizing temperature of the parent gas. Figure 1-3 shows the variation of the electrical conductivity of hydrogen, seeded with 0.1% cesium by mole, with temperature (assuming thermal equilibrium) at different pressures. Notice the relatively high values of conductivity at temperatures as low as $3000K$, which is well below the ionizing temperature of hydrogen ($T_e > 7000K$). The energy coupling between the gas and the electrons could also be weak leading to thermal nonequilibrium, with the gas cooler than the electrons, resulting in gas temperatures low enough to preclude H_2 dissociation.

Exploitation of these effects in a hydrogen arcjet would lead to a significant reduction in frozen losses, e.g. from $13.6eV + 2.3eV$ per ion (H) to $3.89eV$ per ion (C_s). In addition, the device can be designed to operate at lower chamber pressures, leading to reduction in heat fluxes and shorting risks. The presence of the easily ionizable alkali should also reduce near-electrode losses.

1.4 Thesis Overview

The focus of this research is the development of a theoretical model to investigate the feasibility of alkali seeding of arcjet thrusters. Cesium was chosen as the seed element, because of its low ionization potential, and good electrical conductivity at low temperatures. However, the analyses performed on hydrogen and cesium are easily extendable to other parent-seed combinations as well.

The governing equations for a cesium-seeded hydrogen plasma are derived in chapter two. The gas is assumed to be in nonequilibrium so that the ionization and dissociation processes are modeled via rate equations. Included in the derivation are transport and other important gas properties which are relevant to formulation of the governing equations.

In chapter three, a simplified analysis based on a steady solution of the equations for an inviscid constrictor flow model is discussed. The goal of the analysis is to be able to explore the performance characteristics of a seeded thruster without resorting to full scale

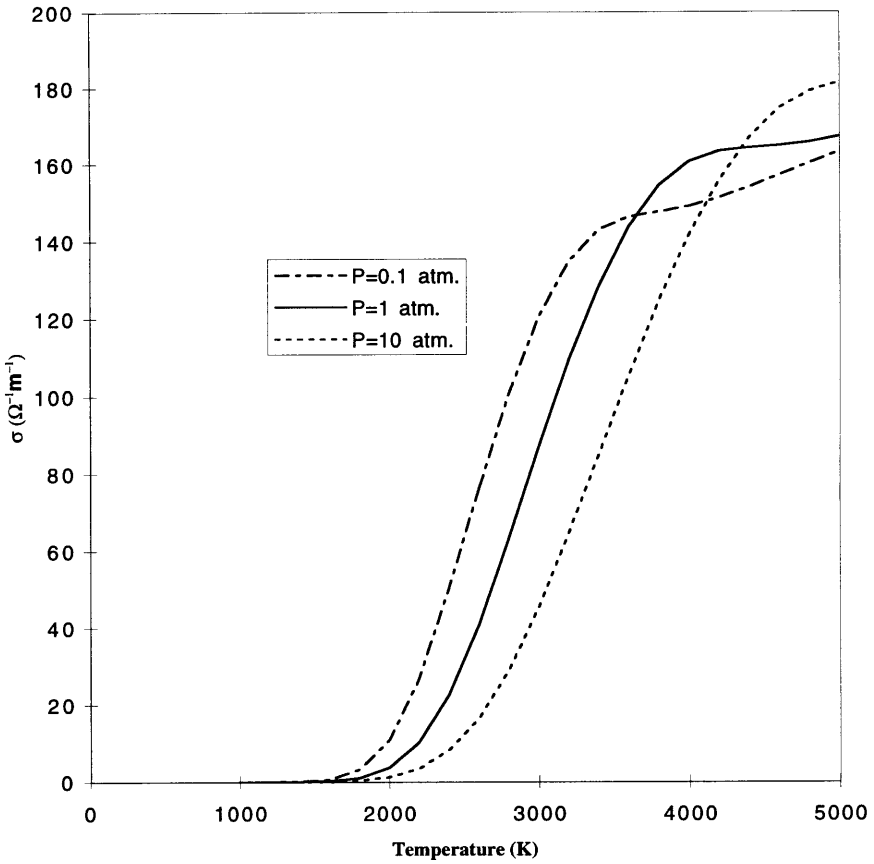

Figure 1-3: Conductivity of hydrogen, seeded with 0.1% cesium per mole

numerical modeling. The model bears resemblance to one developed at MIT by Sakamoto and Martinez-Sanchez for a hydrogen arcjet thruster[9]. The electron temperature was not allowed to exceed $7000K$ in order to prevent the ionization of hydrogen. A constraint was also imposed on the channel length, so as not to incur excessive viscous losses.

At extreme operating conditions, the ionization of hydrogen can no longer be neglected. The presence of hydrogen ions in the system could trigger ionization which in turn could lead into transition to a conventional hydrogen arc. This possibility is investigated in chapter four where a stability analysis is performed on the nonequlibrium governing equations about a uniform background to determine for which values of parameters an instability occurs.

The achievements of this research and recommendation for future research are presented in chapter five.

Chapter 2

Governing Equations

In this chapter, the equations governing the flow in a cesium seeded hydrogen arcjet are presented. These equations are basically the species mass, momentum and energy conservation equations, and the electric potential equation. Also presented in this chapter are the thermal and transport properties of the seeded gas.

2.1 Thermal Properties

The global density of the gas is defined as the sum of the densities of all the species present:

$$\rho = \sum_s \rho_s = \sum_s m_s n_s, \tag{2.1}$$

where m_s and n_s are the mass and number density of species s respectively. The species accounted for in this research are H_2, H, H^+, Cs, Cs^+ and e; effects of molecular ions, H_2^+, and multiple ions of cesium are considered negligible.

The fraction of cesium seed present in the gas is

$$\alpha = \frac{n_{C_s} + n_{C_s^+}}{2n_{H_2} + n_H + n_{H^+}}. \tag{2.2}$$

The electrons are assumed to be maxwellized at a different temperature from the other species, designated as heavy, i.e $T_H = T_{H_2} = T_{H^+} = T_{C_s} = T_{C_s^+} \equiv T \neq T_e$. This assumption allows the electron to be treated as a separate fluid. The gas is assumed be quasi-neutral, so that the electron number density equals the sum of the ion densities,

$$n_e = n_{H^+} + n_{Cs^+}. \tag{2.3}$$

Assuming the gas is ideal, the total pressure is then defined as the sum of the partial pressures of the all the species present,

$$p = \sum_s p_s = \sum_s \rho_s R_s T_s. \tag{2.4}$$

where $R_s = \frac{k_B}{m_s}$ is the gas constant for species s. The quantity k_B is the Boltzmann constant, and equals $1.38 \times 10^{-23} JK^{-1}$. Substituting the expression for R_s, and making use of the quasi-neutrality and two-temperature assumptions, Equation 2.4 can be written as

$$p = (n_H + n_{H_2} + n_{Cs})\, k_B T + n_e k_B\, (T_e + T)\,. \tag{2.5}$$

The above equation is also known as the equation of state.

The enthalpy of the gas is

$$h = \frac{\sum_s n_s h_s}{\rho}, \tag{2.6}$$

where h_s is the enthalpy per molecule of each species s present:

$$h_{H_2} = \frac{7}{2} k_B T - \varepsilon_d + \frac{\varepsilon_{vib}}{e^{\frac{\varepsilon_{vib}}{k_B T}} - 1} + \Delta, \tag{2.7}$$

$$h_H = h_{H^+} = \frac{5}{2} k_B T + \frac{\Delta}{2} \tag{2.8}$$

and

$$h_{Cs} = h_{Cs^+} = \frac{5}{2} k_B\, (T - T_f)\,. \tag{2.9}$$

Here ε_d and ε_{vib} are the dissociation and vibrational excitation energies per molecule respectively, and Δ is a constant chosen so as to make the enthalpy of H_2 zero at the common reference temperature, $T_f = 298.16K$. Since vibrational excitation is negligible at low temperature,

$$\Delta = \varepsilon_d - \frac{7}{2} T_f.$$

The internal energy of the gas is

$$\varepsilon = h - \frac{p}{\rho}. \tag{2.10}$$

2.2 Transport Properties

The transport coefficients of a multicomponent gas are generally obtained from the Chapman-Enskog solution of the Boltzmann equation. A treatment of this solution is too lengthy and mathematically involved to be included in this section; however, it can be found in excellent texts by Chapman and Cowling [3], and Hirschfelder, Curtis and Bird [4]. In this research, the effect of cesium on viscosity and thermal conductivity is considered negligible due to its low mole fraction.

According to the Chapman-Enskog solution, the viscosity and thermal conductivity coefficients for a species s are approximately given by

$$\mu_s = 2.6693 \times 10^{-6} \frac{M_s T_s}{\bar{\Omega}^{(2,2)}} \left[kgm^{-1}s^{-1}\right] \tag{2.11}$$

$$\kappa_s = 8.3227 \times 10^{-5} \frac{T_s/M_s}{\bar{\Omega}^{(2,2)}} = \frac{15}{4}\frac{\hat{R}}{M_s}\mu_s \left[Jm^{-1}s^{-1}K^{-1}\right] \tag{2.12}$$

where M is the molecular weight of species s and $\bar{\Omega}^{(2,2)}$ is the average effective viscosity collision integral.

Equation 2.12 is only valid for monoatomic species. For diatomic species, the Eucken correction is applied to Equation 2.12 to account for internal degrees of freedom[4], so that the conductivity equals

$$\kappa_s = \frac{19}{4}\frac{\hat{R}}{M_s}\mu_s. \tag{2.13}$$

Applying the mixture rule [11], the viscosity and thermal conduction coefficient of a multicomponent gas are

$$\mu = \sum_{i=1}^{s} \frac{n_i \mu_i}{\sum_{j=1}^{s} n_j \chi_{ij}}, \tag{2.14}$$

$$\kappa_g = \sum_{s} \frac{n_s \kappa_s}{\sum_r n_r \chi_{sr}}, \tag{2.15}$$

where

$$\chi_{ij} = \sqrt{\frac{2m_{ij}}{m_i}} \frac{\bar{\Omega}_{ij}^{(2,2)}}{\bar{\Omega}_{ii}^{(2,2)}}. \tag{2.16}$$

The values of the effective average viscosity collision integrals used in this research are given in Appendix A.

The electron thermal conductivity is calculated as [11]

$$\kappa_e = \frac{2.4}{1 + \frac{\nu_{ei}}{\sqrt{2}\nu_e}} \frac{k_B^2 n_e T_e}{m_e \nu_e}. \tag{2.17}$$

In addition to the ordinary thermal conduction, which is due to the transport of kinetic energy during collisions, heats of reaction (ionization and dissociation) are also transported due to diffusion of species from regions of high concentration to regions of lower concentration. This, in fact, is the dominant energy transfer mechanism at temperatures in the dissociation and ionization ranges. Taking this into account, an effective thermal conductivity can be defined as

$$\kappa = \kappa_g + \kappa_{reaction}. \tag{2.18}$$

An approximate expression for $\kappa_{reaction}$ for hydrogen gas due solely to the diffusive transport of heat of dissociation is [8]

$$\kappa_{reaction} = \kappa_{diss} = \frac{n^2 m_H x_H \left(1 - x_{H_2}\right) \left(2h_H - h_{H_2}\right)^2}{\rho \left(1 + x_{H_2}\right) k_B T^2} D_{HH_2}, \tag{2.19}$$

where

$$n = \frac{p}{k_B T} \tag{2.20}$$

and

$$x_s = \frac{n_s}{n}. \tag{2.21}$$

The quantity D_{HH_2} is the diffusion coefficient,

$$D_{HH_2} = \frac{3}{16 p \pi \bar{\Omega}^{(1,1)}} \sqrt{\frac{3k_B T^3}{m_H}} \tag{2.22}$$

where $\bar{\Omega}^{(1,1)}$ is the average effective collision integral for diffusion and is tabulated in Appendix A. The diffusive transport of ionization is considered negligible compared to that of

dissociation, due to the low C_s fraction.

The electrical conductivity of a quasi neutral plasma is defined as[11]:

$$\sigma = \frac{e^2 n_e}{m_e \sum_r \nu_{er}}. \tag{2.23}$$

Here e is the elementary charge (1.602×10^{-19}). The quantity ν_{er} is the collision frequencies of the electrons with heavy species r, and is defined as

$$\nu_{er} = n_r g_{er} Q_{er}, \tag{2.24}$$

where g_{er} and Q_{er} are the mean relative speed and the average momentum transfer collision cross section of the colliding species. Because the electron mass is much smaller than that of the heavy species, the mean relative speed can be approximated as the electron mean thermal speed given as

$$c_e = \sqrt{\frac{8 k_B T_e}{\pi m_e}} \tag{2.25}$$

The interaction between the electrons and ions are Coulombic. The collision cross section for a Coulombic interaction is approximately given as[11]

$$Q_{ei} = 6\pi \bar{b}_0^2 ln\Lambda \tag{2.26}$$

where $ln\Lambda$ is known as the Spitzer logarithm and is shown in 2.1.

Table 2.1: Values of $ln\Lambda$

T_e, K	n_e, m^{-3}			
	10^{15}	10^{18}	10^{21}	10^{24}
10^2	9.43	5.97	-	-
10^3	12.8	9.43	5.97	-
10^4	16.3	12.8	9.43	5.97
10^5	19.7	16.3	12.8	9.43

The constant $\bar{b}_0$ is calculated as

$$\bar{b}_0 = \frac{5.56 \times 10^{-6}}{T_e} \tag{2.27}$$

The collision cross sections for relevant electron hydrogen interactions used in this research are given in Appendix A, while those of electron-cesium interactions are shown in Fig. 2-1, taken from Ref. [2].

Comparison of ν_{eC_s} to ν_{eH_2},

$$\frac{\nu_{eC_s}}{\nu_{eH_2}} = \frac{n_{C_s} Q_{eC_s}}{n_{H_2} Q_{eH_2}} \sim \alpha \frac{Q_{eC_s}}{Q_{eH_2}},$$

shows that the effect of $e - C_s$ collisions is negligible compared to that of $e - H_2$ collisions, since the above ratio is always less than unity for all the cases treated in this research ($\alpha \ll 1$).

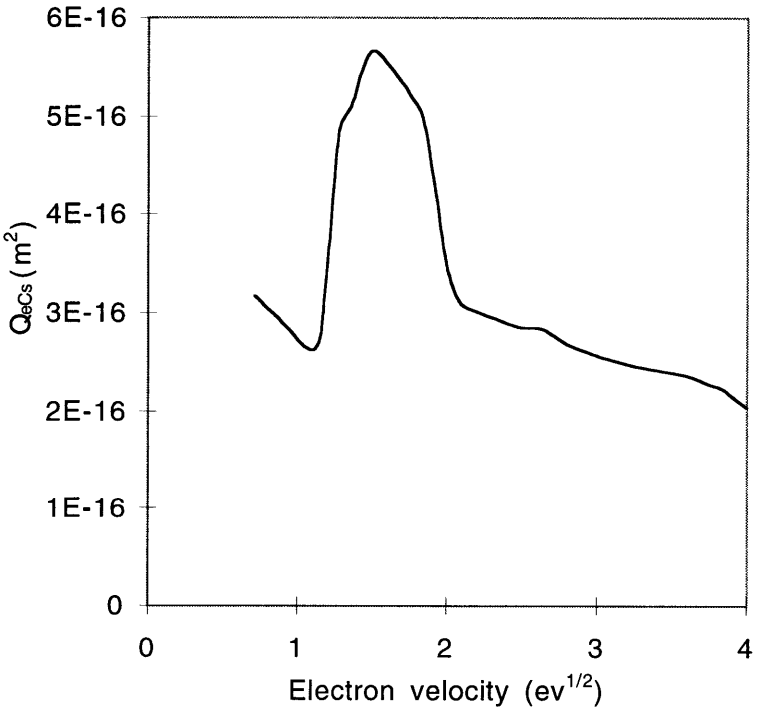

Figure 2-1: Electron-Cesium momentum transfer collision cross section

2.3 Flow Chemistry

2.3.1 Dissociation

The dissociation of molecular hydrogen occurs as a result of inelastic collisions with a second body, whose energy is in excess of its dissociation energy ($4.478eV$ or $7.174 \times 10^{-19}J$ per molecule):

$$H_2 + M \rightleftharpoons H + H + M \tag{2.28}$$

The third body, M, can be any of the heavy species, electrons or photons (photodissociation) present. In arcjets, the dominant collisional processes responsible for dissociation are mainly by atomic and molecular hydrogen, and electrons; photodissociation is generally infrequent. The inverse reaction is known as three body recombination. In typical arcjet flow regions, the effect of electron impact molecular recombination is negligible[6]. The net dissociation rate of molecular hydrogen due to heavy species collisions, based on a model developed by Rogers et al.[13] is given by

$$\dot{n}_{H_{heavy}} = (5n_H + 2n_{H_2}) \left(K_f n_{H_2} - K_b n_H^2 \right), \tag{2.29}$$

where K_f and K_b are the forward and backward rates respectively, and are related through the equilibrium constant:

$$K_b = \frac{K_f}{K_n} \tag{2.30}$$

The forward rate is defined as

$$K_f = \frac{AN_{AV}}{T} \exp\left(-\frac{B}{\hat{R}T} \right) \tag{2.31}$$

The equilibrium constant, $K_n(T)$, is calculated as:

$$K_n(T) = \frac{q_H^2}{q_{H_2}} \tag{2.32}$$

The atomic and molecular partition functions are defined respectively as:

$$q_H = q_H^{tr} e^{-\frac{\Delta}{2k_B T}} \tag{2.33}$$

$$q_{H_2} = 2^{\frac{3}{2}} q_H^{tr} \frac{T}{2\theta_r} \frac{e^{\frac{\epsilon_d - \Delta}{k_B T}}}{1 - e^{-\frac{\epsilon_v}{k_B T}}}, \tag{2.34}$$

where q_H^{tr} is the translational partition function,

$$q_H^{tr} = \left(\frac{2\pi m_H kT}{h^2}\right)^{\frac{3}{2}}. \tag{2.35}$$

Here $\epsilon_r = 87.5K$ is the temperature corresponding to rotational excitation of hydrogen molecules.

The production rate due to electron impact is

$$\dot{n}_{H_{electron}} = K_{e_{H_2}} n_e n_{H_2}, \tag{2.36}$$

where $K_{e_{H_2}}$ is the reaction rate coefficient, and is taken from Janev et al.[6] and plotted in Figure 2-2. Typically, the production rate due to electron impact is negligible to that due to heavy impact at electron temperatures below $10000K$.

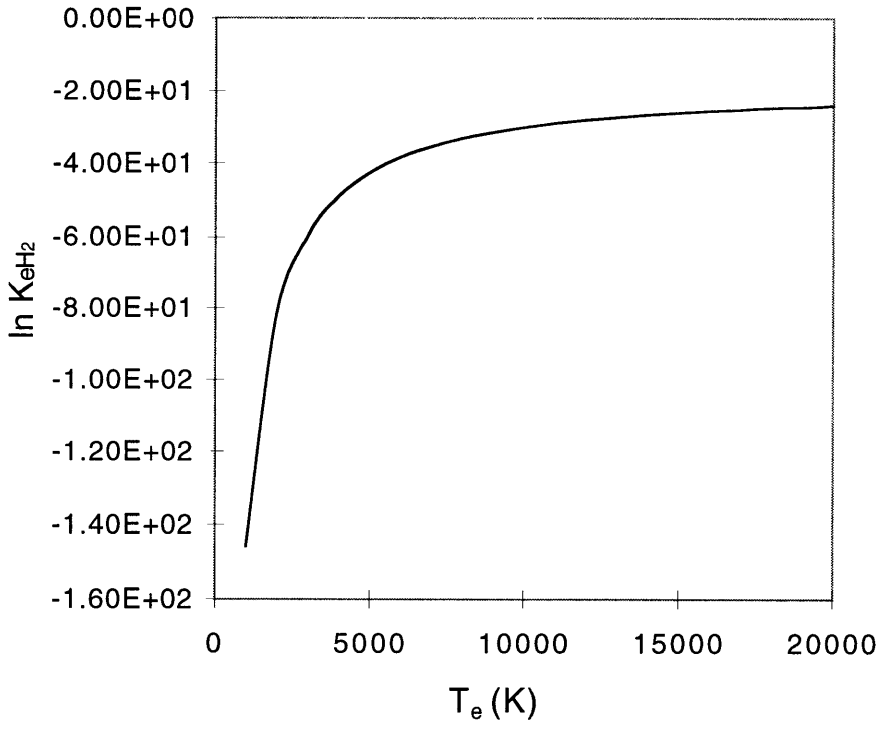

Figure 2-2: Reaction Rate Coefficient for $e - H_2$ Dissociating Collisions

2.3.2 Ionization

The ionization reactions considered in this research are of the form:

$$A + e \rightleftharpoons A^+ + e + e, \tag{2.37}$$

where $A = H$ and C_s. The net ion production rate of species A due to ionization and three body recombination is[11]

$$\dot{n}_{A^+} = R_{Sh} n_e \left(S_A n_A - n_e n_{A^+} \right), \tag{2.38}$$

where the recombination rate coefficient as modified by Sheppard[15]

$$R_{Sh} = 6.985 \times 10^{-42} \exp \left[\frac{\left(\ln \frac{T_e}{1000} - 4.0833 \right)^2}{0.8179} \right] \quad \left[\mathrm{m}^3/\mathrm{s} \right]. \tag{2.39}$$

is used, as opposed to the commonly used Hinnov-Hirschberg coefficient,

$$R_{HH} = \frac{1.09 \times 10^{-20}}{T_e^{\frac{9}{2}}} \quad \left[\mathrm{m}^3/\mathrm{s} \right], \tag{2.40}$$

which was shown by Sheppard to overpredict the recombination rates at high electron temperatures. The Saha function, S_A, is defined as

$$S_A = 2 \frac{g_{A^+}}{g_A} \left(\frac{2\pi m_e k_B T_e}{h^2} \right)^{\frac{3}{2}} e^{-\frac{\varepsilon_{i_A}}{k_B T_e}}, \tag{2.41}$$

where g_A is the degeneracy of species A, ε_{i_A} is the ionization potential of monoatomic species A and h is the Planck's constant.

2.4 Continuity Equations

The law of conservation of species requires that the rate per unit volume of species accumulation be balanced by the rates of depletion or formation and the net outflow per unit volume i.e.

$$\frac{\partial \rho_s}{\partial t} + \nabla \cdot (\rho_s \vec{v_s}) = m_s \dot{n}_s. \tag{2.42}$$

The volumetric rates of production (or depletion) of all the species, based on the discussions of the previous section, are

$$\dot{n}_{H^+} = R_{Sh} n_e \left(S_H n_H - n_e n_{H^+}\right) \tag{2.43}$$

$$\dot{n}_{C_s^+} = R_{Sh} n_e \left(S_{C_s} n_{C_s} - n_e n_{C_s^+}\right) \tag{2.44}$$

$$\dot{n}_{C_s} = -\dot{n}_{C_s^+} \tag{2.45}$$

$$\dot{n}_{H_2} = -\frac{1}{2}\left[K_f \left(5n_H + 2n_{H_2}\right)\left(n_{H_2} - \frac{n_H^2}{K_n}\right) + K_{e_{H_2}} n_e n_{H_2}\right] \tag{2.46}$$

$$\dot{n_H} = -2\dot{n}_{H_2} - \dot{n}_{H^+} \tag{2.47}$$

$$\dot{n}_e = \dot{n}_{H^+} + \dot{n}_{C_s^+} \tag{2.48}$$

The global continuity equation is then obtained by summing Equation 2.42 over all species present,

$$\frac{\partial \rho}{\partial t} + \nabla \cdot (\rho \vec{v}) = 0, \tag{2.49}$$

where the total sum of net volumetric rate production,

$$\sum_s \dot{n}_s = 0,$$

and definitions of global density and the mean flow velocity have been used.

2.5 Momentum Equations

The species momentum equation relates the rate of change of momentum of each species to the different forces acting on it. The forces acting can be divided into two parts: body forces, gravity and Lorentz (electromagnetic) forces; and surface forces, pressure and shear forces. In plasmas generally, the effect of gravitational forces is negligible when compared to those of electromagnetic and surface forces. Neglecting gravity, the momentum equation for each species is given as

$$\left[\frac{\partial \left(m_s n_s \vec{v_s}\right)}{\partial t} + \left(\vec{v_s} \cdot \nabla\right) \vec{v_s}\right] + m_s n_s \sum_s \nu_{sr} \left(\vec{v_s} - \vec{v_r}\right) = -\nabla \cdot \bar{\bar{p}}_s + n_s Z_s \left(\vec{E} + \vec{v_s} \times \vec{B}\right) \tag{2.50}$$

Here Z_s is the species charge and $\overline{\overline{p}}_s$ is the kinetic pressure dyad defined as

$$\overline{\overline{p}}_s = p_s \overline{\overline{I}} - \tau_s, \tag{2.51}$$

where $\overline{\overline{I}}$ is the identity tensor and τ_s is the viscous stress tensor. The last term on the left hand side of Equation 2.50 denotes the collisional rate of change of mean momentum for species s.

A further simplification of the momentum equation for the electrons can be made by neglecting inertial and viscous terms, and defining current density as $\vec{j} = en_e(\vec{v_i} - \vec{v_e})$,

$$\sigma\left(\vec{E} + \vec{v_s} \times \vec{B}\right) = \vec{j} + \vec{j} \times \vec{\beta} - \zeta \nabla p_e \tag{2.52}$$

The resulting equation is the generalized form of Ohm's law. The Hall parameter, β, is the ratio between the cyclotron frequency and the collision frequency,

$$\beta = \frac{eB}{m_e \nu_e}. \tag{2.53}$$

The quantity ζ is the electron mobility,

$$\zeta = \frac{e}{m_e \nu_e}. \tag{2.54}$$

In low power arcjets, the effect of the magnetic field is generally negligible, so that the generalized Ohm's law simplifies to

$$\vec{j} = \sigma \vec{E} + \zeta \nabla p_e. \tag{2.55}$$

A global momentum equation is then obtained by summing equation 2.50 for all the species; if $B = 0$, this gives

$$\frac{\partial \rho \vec{v}}{\partial t} + \nabla \cdot (\overline{\overline{p}} + \rho \vec{v}\vec{v}) = 0. \tag{2.56}$$

Where the equation of state and the definitions of global density and mean flow velocity have been used. The collisional and Lorentz force terms all cancel out during the summation.

2.6 Energy Equations

Two separate energy equations are needed because of the two-temperature assumption made: one for the electrons and the other for the heavy species.

Electrons

The electron energy equation is a balance between energy input to the electrons through Joule heating, $\vec{j} \cdot \vec{E}$, and losses via collisions with the heavy species, E_{coll}, heat diffusion and convection, and volumetric radiation, $\dot{R}$:

$$\frac{\partial}{\partial t}\left(\frac{3}{2}k_B T_e + m_e v_e^2 + \varepsilon_{i_H} + \varepsilon_{i_{C_s}}\right) n_e + \nabla \cdot \left[\left(\frac{5}{2}k_B T_e + m_e v_e^2 + \varepsilon_{i_H} + \varepsilon_{i_{C_s}}\right) n_e \vec{v_e}\right]$$

$$-\nabla \cdot (\kappa_e \nabla T_e) = \vec{j} \cdot \vec{E} - E_{coll} - \dot{R}, \tag{2.57}$$

where ε_H and ε_{C_s} are the ionization energy per atom of hydrogen and cesium respectively.

The collisional energy transfer, E_{coll} is given as

$$E_{coll} = 3 m_e n_e k_B \left(T_e - T\right) \sum_s \frac{\nu_{es} \delta_s \left(T_e\right)}{m_s}, \tag{2.58}$$

where $\delta_s \left(T_e\right)$ is the inelastic collision correction factor ($\delta = 1$ for monoatomic species) and is plotted for hydrogen and other polyatomic species in Fig. 2-3[16].

Heavy Species

The heavy species energy equation takes into account the energy imparted to the heavy species through collisions with electrons, and energy transfer through conduction and convection,

$$\frac{\partial}{\partial t}\left(\rho\varepsilon + \frac{1}{2}\rho v^2\right) + \nabla \cdot \vec{v}\left(\rho h + \frac{1}{2}\rho v^2\right) - \nabla \cdot (\kappa \nabla T) = E_{coll}. \tag{2.59}$$

2.7 Electric Potential Equation

The electric potential equation is obtained from the generalized Ohm's law, Equation 2.55, and Maxwell's equations of electromagnetism. Maxwell's equations for a quasi neutral

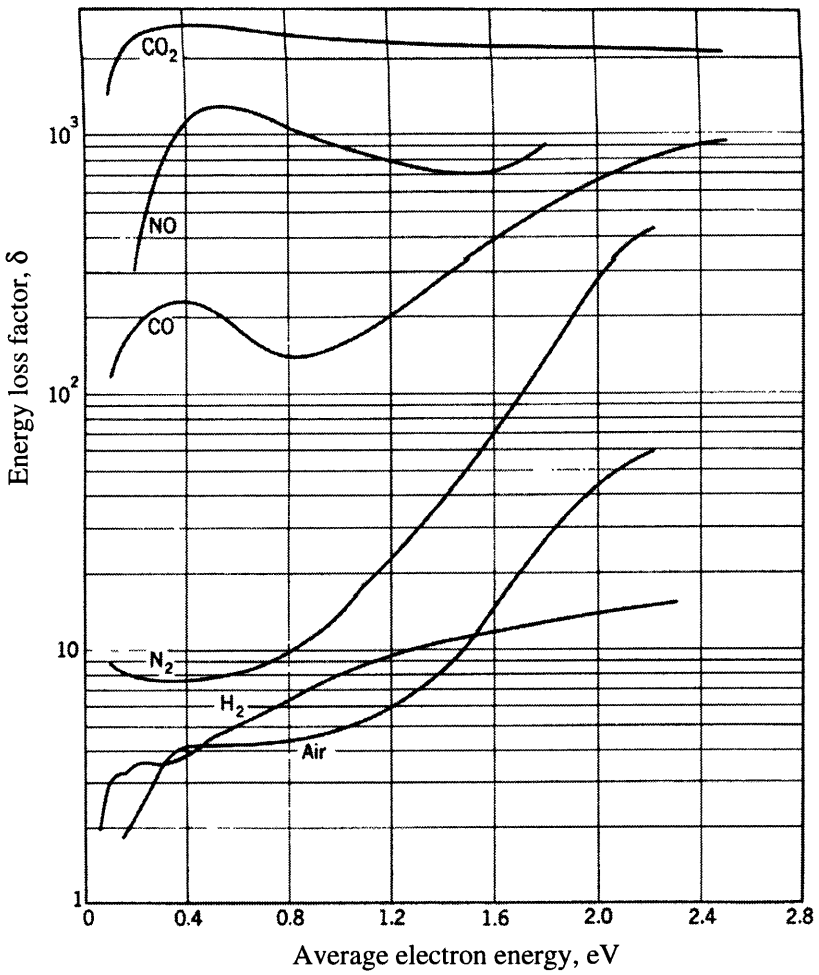

Figure 2-3: Inelastic collision correction factor for some polyatomic species

plasma in the absence of magnetic field reduce to

$$\nabla \cdot \vec{E} = 0, \tag{2.60}$$

$$\nabla \times \vec{E} = 0, \tag{2.61}$$

$$\nabla \cdot \vec{j} = 0. \tag{2.62}$$

Equation 2.61 implies that the electric field can be written as the gradient of a scalar potential:

$$\vec{E} = -\nabla\phi \tag{2.63}$$

Substituting equations 2.55 and 2.63 into 2.62,the final expression for the electric potential equation is obtained

$$\nabla \cdot (\zeta \nabla p_e) - \nabla \cdot (\sigma \nabla \phi) = 0 \tag{2.64}$$

Chapter 3

A Simplified Flow Analysis

In this chapter, a simplified model based on steady state approximations to the governing equations for inviscid flow in the constrictor is presented. The electron temperature is not allowed to exceed $7000K$ so as to exclude the presence of H^+. A restriction was also imposed on the length of the constrictor so as not to incur excessive viscous losses. The ionization and dissociation processes are modeled in equilibrium. The model does not account for near-electrode effects and nozzle flow, which is simply taken to be frozen isentropic with the arc attaching at the constrictor exit. It was able, however, to explore the operation of a seeded thruster without necessarily complicating the physics, and should serve as a foundation for further advanced studies. The nonequilibrium treatment is given in the next chapter on stability analysis.

In the absence of H^+, Equations 2.2 and 2.3 respectively reduce to

$$\alpha = \frac{n_{C_s} + n_{C_s^+}}{n_H + 2n_{H_2}} \tag{3.1}$$

and

$$n_e = n_{C_s^+} \tag{3.2}$$

3.1 Ionizational and Dissociative Equilibrium

Implicit in the equilibrium assumption of steady state, is the dominance of collisional processes over their radiative counterpart. This is generally valid at very high density, when the gas can be considered to be optically thick. In equilibrium, the forward rate is exactly

balanced by the backwards rate of reaction, and as a result, for the ionization process, the number densities of the electrons, cesium atoms and ions are related by the Saha equation:

$$\frac{n_e n_{Cs^+}}{n_{Cs}} = \left(\frac{2\pi m_e k T_e}{h^2}\right)^{\frac{3}{2}} e^{-\frac{\epsilon_{i_{Cs}}}{kT_e}}. \tag{3.3}$$

For the dissociation process at equilibrium, the law of mass action requires that the number densities of hydrogen species be related by

$$\frac{n_H^2}{n_{H_2}} = K_n(T) \tag{3.4}$$

3.2 Steady Flow Equations

The analysis carried out in this section is focused on quasi one dimensional flow in a constrictor of cylindrical geometry. Quasi one dimensionality in this case implies that the radial and azimuthal components of the velocity and electric field are negligible; however, the radial heat conduction is retained, and in fact is assumed to dominate over axial conduction. In addition, pressure and the axial component of the electric field are assumed radially uniform. A direct consequence of uniform pressure is the corresponding radial uniformity in the momentum flux in the absence of viscous effects. This allows the definition of a quantity q as

$$q(x) = \rho v^2, \tag{3.5}$$

so that

$$\rho v = \sqrt{\rho q} \tag{3.6}$$

For simplicity, all the heavy species are assumed to travel at the same velocity except for the effect of ambipolar diffusion which has been incorporated into the transport mechanism.

At steady state, the continuity equation, Equation 2.49 reduces to

$$\nabla \cdot (\rho \vec{v}) = 0 \tag{3.7}$$

Integrating over the volume of the cylinder gives:

$$\int_V \nabla \cdot (\rho \vec{v})\, dV = 0 \tag{3.8}$$

Converting to a surface integral by applying the divergence theorem:

$$\int_V \nabla \cdot (\rho \vec{v})\, dV = \int_S \rho \vec{v} \cdot \vec{n}\, dS = 0 \tag{3.9}$$

where $\vec{n}$ is the normal to the control surface. The above equation implies that, at steady state, the mass flow rate is a constant:

$$\dot{m} = \int_0^R \sqrt{\rho q} 2\pi r\, dr = const, \tag{3.10}$$

Similar operations on the momentum and potential equation yield an integral statement of the conservation of momentum and current:

$$\int_0^R (p + \rho v^2) 2\pi r\, dr = J = const \tag{3.11}$$

$$E \int_0^R 2\pi\sigma\, dr = I = const. \tag{3.12}$$

where the constant J and I are the impulse and arc current respectively.

Differentiation of Equations 3.10, 3.11 and 3.12 with respect to x yields:

$$\frac{1}{2\sqrt{q}} \left(\int_0^R 2\pi r \sqrt{\rho}\, dr \right) \frac{dq}{dx} + \sqrt{q} \int_0^R \frac{2\pi r}{2\sqrt{\rho}} \left(\frac{\partial \rho}{\partial x} \right) dr + 2\pi R \sqrt{q\rho} \frac{dR}{dx} = 0 \tag{3.13}$$

$$\frac{d}{dx}(p+q) \int_0^R 2\pi r\, dr + 2\pi R\,(p+q) \frac{dR}{dx} = 0 \tag{3.14}$$

$$\left(\int_0^R r\sigma\, dr \right) \frac{dE}{dx} + E \int_0^R r \left(\frac{\partial \sigma}{\partial x} \right) dr + 2\pi R E \sigma\,(R) \frac{dR}{dx} = 0 \tag{3.15}$$

where the radial uniformity of pressure and momentum flux has been exploited. For a constant area channel,

$$\frac{dR}{dx} = 0 \tag{3.16}$$

As a result, Equations 3.13-3.15 become

$$\frac{1}{2\sqrt{q}} \left(\int_0^R 2\pi r \sqrt{\rho}\, dr \right) \frac{dq}{dx} + \sqrt{q} \int_0^R \frac{2\pi r}{2\sqrt{\rho}} \left(\frac{\partial \rho}{\partial x} \right) dr = 0 \tag{3.17}$$

$$\frac{dp}{dx} = -\frac{dq}{dx} \tag{3.18}$$

$$\left(\int_0^R r\sigma\, dr\right)\frac{dE}{dx} + E\int_0^R r\left(\frac{\partial\sigma}{\partial x}\right) dr = 0 \tag{3.19}$$

The electron temperature is related to the gas temperature through the electron energy balance at steady state:

$$\frac{j^2}{\sigma} = 3\frac{m_e}{m_H} n_e k_B \left(T_e - T\right)\left(\nu_{eH} + \nu_{eH_2}\frac{\delta_{H_2}}{2}\right) \tag{3.20}$$

where ionization work has been neglected, since cesium is almost fully ionized at the temperatures considered. Neglecting electron pressure forces compared to electrical forces, Ohm's law, Equation 2.55, reduces to

$$\vec{j} = \sigma\vec{E} \tag{3.21}$$

Substituting for j in Equation 3.20, after rearrangement, yields a quadratic equation in $\frac{T_e}{T}$:

$$\left(\frac{T_e}{T}\right)^2 - \frac{T_e}{T} - \frac{(E/p)^2}{8.00\times 10^{34}\delta_{H_2} f_1 f_2} = 0 \tag{3.22}$$

where

$$f_1 = 1 + \frac{n_e Q_{ei}}{n_H Q_{eH_2}} \tag{3.23}$$

$$f_2 = 1 + \frac{m_{H_2} n_e Q_{ei}}{\delta_{H_2} m_{cs} n_H Q_{eH_2}} \tag{3.24}$$

An approximate 2-D steady state energy equation of the gas, neglecting radial convection and axial conduction, is

$$\rho v\frac{\partial h_t}{\partial x} = \frac{1}{r}\frac{\partial}{\partial r}\left(r\kappa\frac{\partial T}{\partial r}\right) + \sigma E^2 \tag{3.25}$$

Because the thermal conductivity is generally a rapidly varying function of temperature, a common practice is to introduce the heat flux potential defined as

$$\varphi = \int^T \kappa\, dT,$$

so that,

$$\kappa\frac{\partial T}{\partial r} = \frac{\partial\varphi}{\partial r}$$

substituting the above expression into the energy equation and exploiting the radial

uniformity in momentum flux, leads to an equation of the form:

$$\frac{\partial h_t}{\partial x} = \frac{1}{\sqrt{q\rho}}\left[\frac{1}{r}\frac{\partial}{\partial r}\left(r\frac{\partial \varphi}{\partial r}\right) + \sigma E^2\right] \tag{3.26}$$

The governing equations are further simplified by expressing enthalpy, conductivity and density as functions of T and P, so that their partial derivatives with respect to x are

$$\frac{\partial h}{\partial x} = \left(\frac{\partial h}{\partial T}\right)_p \frac{\partial T}{\partial x} + \left(\frac{\partial h}{\partial p}\right)_T \frac{dp}{dx} \tag{3.27}$$

$$\frac{\partial \rho}{\partial x} = \left(\frac{\partial \rho}{\partial T}\right)_p \frac{\partial T}{\partial x} + \left(\frac{\partial \rho}{\partial p}\right)_T \frac{dp}{dx} \tag{3.28}$$

$$\frac{\partial \sigma}{\partial x} = \left(\frac{\partial \sigma}{\partial T}\right)_p \frac{\partial T}{\partial x} + \left(\frac{\partial \sigma}{\partial p}\right)_T \frac{dp}{dx} \tag{3.29}$$

Substituting the expression for $\frac{\partial \sigma}{\partial x}$ in Equation 3.19, after rearranging gives:

$$\frac{dE}{dx} = -\frac{E\int_0^R r\left[\left(\frac{\partial \sigma}{\partial T}\right)_p \frac{\partial T}{\partial x} + \left(\frac{\partial \sigma}{\partial p}\right)_T \frac{dp}{dx}\right] dr}{\int_0^R r\sigma dr} \tag{3.30}$$

The total enthalpy, h_t, is defined as

$$h_t = h + \frac{v^2}{2} = h + \frac{q}{2\rho} \tag{3.31}$$

Differentiating with respect to x, leads to

$$\frac{\partial h_t}{\partial x} = \frac{\partial h}{\partial x} + \frac{1}{2\rho}\frac{dq}{dx} - \frac{q}{2\rho^2}\frac{\partial \rho}{\partial x} \tag{3.32}$$

Substituting for $\frac{\partial h}{\partial x}$, $\frac{\partial \rho}{\partial x}$ and $\frac{dq}{dx}$ from Equations 3.27, 3.28 and 3.18 respectively, the above equation becomes

$$\frac{\partial h_t}{\partial x} = \left(\frac{\partial h}{\partial T}\right)_p \frac{\partial T}{\partial x} + \left(\frac{\partial h}{\partial p}\right)_T \frac{dp}{dx} - \frac{1}{2\rho}\frac{dp}{dx} - \frac{q}{2\rho^2}\left[\left(\frac{\partial \rho}{\partial T}\right)_p \frac{\partial T}{\partial x} + \left(\frac{\partial \rho}{\partial p}\right)_T \frac{dp}{dx}\right] \tag{3.33}$$

Making $\frac{\partial T}{\partial x}$ the subject of the formula, leads to

$$\frac{\partial T}{\partial x} = \frac{\frac{\partial h_t}{\partial x} + \vartheta\frac{dp}{dx}}{\xi} \tag{3.34}$$

where

$$\vartheta = \frac{1}{2\rho} - \left(\frac{\partial h}{\partial p}\right)_T + \frac{q}{2\rho^2}\left(\frac{\partial \rho}{\partial p}\right)_T \tag{3.35}$$

$$\xi = \left(\frac{\partial h}{\partial T}\right)_p - \frac{q}{2\rho^2}\left(\frac{\partial \rho}{\partial T}\right)_p \tag{3.36}$$

Substituting the above expression for $\frac{\partial T}{\partial x}$ into Equation 3.28 gives

$$\frac{\partial \rho}{\partial x} = \left(\frac{\partial \rho}{\partial T}\right)_p \frac{\frac{\partial h_t}{\partial x} + \vartheta \frac{dp}{dx}}{\xi} + \left(\frac{\partial \rho}{\partial p}\right)_T \frac{dp}{dx} \tag{3.37}$$

Substituting Equations 3.37 and 3.18 into 3.17, after rearranging, we obtain

$$\frac{dp}{dx} = \frac{\int_0^R \frac{r}{\xi\sqrt{\rho}}\left(\frac{\partial \rho}{\partial T}\right)_p \frac{\partial h_t}{\partial x} dr}{\frac{1}{q}\int_0^R r\sqrt{\rho} dr - \int_0^R \frac{r}{\sqrt{\rho}}\left[\frac{\vartheta}{\xi}\left(\frac{\partial \rho}{\partial T}\right)_p + \left(\frac{\partial \rho}{\partial p}\right)_T\right] dr} \tag{3.38}$$

Equations 3.38 and 3.30 are independent of the radius, while Equations 3.26 and 3.34 have to be evaluated at each axial and radial point. These equations are then integrated downstream for a fixed constrictor geometry, seed fraction, current, and prescribed inlet and boundary conditions, until the flow becomes choked. The choking point is taken to be the end of the constrictor, since the flow undergoes rapid expansion after that. The physical domain of interest is shown in Figure 3-1.

3.3 Method of Solution

3.3.1 Initial and Boundary Conditions

The quantities prescribed at the inlet are the total pressure, p_t, the inlet Mach number, M_0, and an arbitrary inlet radial temperature profile of the form:

$$T(r) = T_w + (T_c - T_w)\left[1 - \left(\frac{r}{r_{con}}\right)^5\right] exp\left[-\left(\frac{1.5r}{r_{cat}}\right)^2\right], \tag{3.39}$$

where T_w and T_c are the wall and core temperatures respectively, r_{con} and r_{cat} are respectively the constrictor and cathode radii. Based on these prescribed quantities, Equations 2.5, 3.2, 3.1, 3.3, 3.4 and 3.20 are then solved to yield the species number densities, electron temperature distribution and the electric field at the inlet.

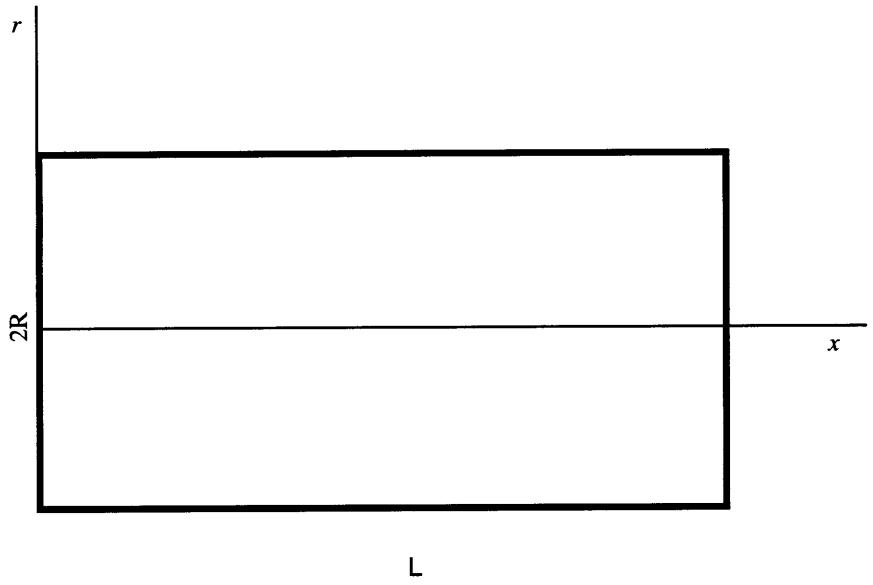

Figure 3-1: Physical domain

A symmetry boundary condition is imposed at core of the arc,

$$\left(\frac{\partial T}{\partial r}\right)_{r=0} = 0 \tag{3.40}$$

At the walls, an insulating boundary condition is imposed, so that

$$\left(\kappa\frac{\partial T}{\partial r}\right)_{r=R} = 0 \tag{3.41}$$

A sonic condition is specified at the constrictor exit. This implies that the pressure gradient at the exit is infinite, and is implemented by setting the denominator of Equation 3.38 to zero, i.e.

$$\frac{1}{q}\int_0^R r\sqrt{\rho}dr - \int_0^R \frac{r}{\sqrt{\rho}}\left[\frac{\vartheta}{\xi}\left(\frac{\partial\rho}{\partial T}\right)_p + \left(\frac{\partial\rho}{\partial p}\right)_T\right]dr = 0 \tag{3.42}$$

3.3.2 Procedure

The gas is assumed to undergo isentropic expansion from its initial state (p_0 and T_0) to the Mach number specified at the inlet. As a result of electron heating at the cathode, the temperature is then assumed to be distributed according to Equation 3.39.

At every radial station i, $\frac{\partial h_t}{\partial x}(r)$ in equation 3.26 is computed as

$$\left(\frac{\partial h_t}{\partial x}\right)_i = \frac{1}{\sqrt{q\rho_i}}\left[\frac{r_{i+\frac{1}{2}}(\varphi_{i+1}-\varphi_i) - r_{i-\frac{1}{2}}(\varphi_i - \varphi_{i-1})}{r_i \Delta r^2} + \sigma_i E^2\right] \tag{3.43}$$

In order to avoid the mathematical singularity associated with the above equation at $r = 0$, the heat flux potential at this point is approximated by a cubic polynomial.

Substituting Equation 3.43 into Equation 3.38 and integrating numerically along the radial direction, $\frac{dp}{dx}$ is obtained. This along with $\frac{\partial h_t}{\partial x}$, is used to determine $\frac{\partial T}{\partial x}$ (Eq. 3.34), which is then used to determine $\frac{dE}{dx}$ (Eq. 3.30), through additional radial integration. The step size is determined by local stability condition,

$$\Delta_x \leq \frac{(\Delta r)^2}{2\aleph_{max}} \tag{3.44}$$

where Δr is the radial grid spacing, and $\aleph_{max}$ is the maximum of the counterflow heat diffusion length

$$\aleph \equiv \frac{heat\ diffusivity}{velocity} = \frac{\kappa}{\sqrt{q\rho}\frac{\partial h}{\partial T}}$$

computed at every radial station i.

Once P, T and E have been determined at one grid point, enthalpy and other variables can be computed as well. The above steps are then repeated until sonic conditions are reached. Arc attachment is assumed to occur at the constrictor exit.

3.3.3 Performance

For the sake of simplicity, the gas is assumed to expand in the diverging nozzle which follows the constrictor to a Mach number of 5, which is a reasonable assumption for arcjet flows. The thrust and specific impulse for a frozen nozzle expansion can be calculated approximately as

$$F = C_{th} p_{t_{throat}} A_{con} \tag{3.45}$$

$$I_{sp} = \frac{F}{\dot{m}g} \tag{3.46}$$

where $p_{t_{throat}}$ is the stagnation pressure at the sonic point, A_{con} is the constrictor cross section area and C_{th} is the thrust coefficient, taken to be approximately $1.8(\gamma = 1.3, M_{exit} =$

Table 3.1: Typical Results

Case	1	2	3	4	5	6	7
Radius, *mm*	1.2		1.4				
Input Mach No.	0.20	0.25	0.22	0.22	0.22	0.22	0.3
Current, *A*	10	10	14	19	17	17	17
Total Pressure, *atm*	3	2	3.3	3.3	3.3	3.3	3.3
Seed Fraction per mole, 10^-4	3	3	3	3	4	3	3
Specific Impulse, *sec*	906	746	834	836	835	835	682
Voltage, V	792	379	724	537	597	595	425
Frozen Losses, %	4	0.03	1.3	0.9	1.3	1	0
L/D	17	8.7	13	6.8	10.5	8.7	6.3
$T_{e_{max}}$	6330	6765	5760	7623	5834	6800	6123

5). The frozen losses are defined as

$$E_{frozen} = n_H \frac{\epsilon_d}{2} c A_{con} \tag{3.47}$$

where c is the exit gas velocity, and n_H is the radial mean density at the same point.

3.4 Discussion of Results

A numerical code in C was developed to solve the problem. Thruster parameters were chosen based on previous results obtained from hydrogen arcjet thruster modeling. These parameters were chosen in such a way as to maximize performance without violating the temperature and geometrical constraints of the model. Typical results obtained for inlet wall temperature of $400K$ and cathode tip temperature of $3500K$ are displayed in Table 3.1. The cathode radius is taken to equal one-quarter of the constrictor radius. An important observation made is the dependence of the exit conditions, hence performance, on the inlet temperature distribution. Although this dependence is not strong, it is is one of the limitations of the model, and can only be rectified by an advanced model, which takes into consideration the physics around the cathode.

In order to identify operational trends, Case 6 in Table 3.1 was selected as a nominal case. Computations were then made in a parametric fashion, varying only one of the major parameters at a time (seed fraction, chamber pressure, current and inlet Mach number), while keeping all else constant. The results are shown in Figures 3-2 through 3-9.

Most of the trends shown by these numerical results can be understood with reference

to a simple model of heat addition to a gas in a constant area duct. The conservation equations for this situation, written between the duct inlet and its choked exit, are

$$\rho_* u_* = \rho_0 u_0 = \sqrt{\frac{\gamma}{R_g T_{t_0}}} p_{t_0} M_0 \tag{3.48}$$

$$p_* + \rho_* u_*^2 = p_0 + \rho_0 u_0^2 \approx p_{t_0} \tag{3.49}$$

$$c_p T_* + \frac{1}{2} u_*^2 = c_p \left(T_{t_0} + \Delta T_t\right) \tag{3.50}$$

where $c_p \Delta T_t$ is the amount of heat added per unit mass. In addition $u_*^2 = \gamma R_g T_*$ and $\frac{P_*}{\rho_*} = R_g T_*$. The approximations in the right side of Eqs. 3.48 to 3.50 are valid for small M_0. Solving the above system for ΔT_t, gives

$$\frac{\Delta T_t}{T_{t_0}} = \frac{1}{2\left(\gamma + 1\right) M_0^2} - 1 \tag{3.51}$$

which shows the exit total temperature to be directly proportional to the inlet temperature, but inversely proportional to the square of the Mach number. Since the thruster specific impulse scales as the square root of T_{t_*}, this implies that I_{sp} should vary as $\frac{1}{M_0}$, and be independent of the other parameters. This is confirmed by the results in Figs. 3-2 to 3-9.

The overall power balance for the heated flow is $IV = \dot{m} \Delta h_t$, which can be rewritten as,

$$V = \frac{\rho u \Delta h_t A}{I} \tag{3.52}$$

With reference to Eq 3.51, the voltage must scale as the quantity

$$\frac{p_{t_0}}{I/A} \left(\frac{1}{2\left(\gamma + 1\right) M_0} - M_0 \right) \tag{3.53}$$

which is also confirmed by the numerical results. In particular as Fig. 3-3 illustrates, V is independent of seed fraction. Noting that $V = EL$, and using Ohm's law, $V = \frac{I/A}{\sigma} L$, leads to the conclusion that the constrictor length must scale as

$$\frac{p_{t_0} \alpha}{\left(I/A\right)^2} \left(\frac{1}{2\left(\gamma + 1\right) M_0} - M_0 \right) \tag{3.54}$$

where α is the seed fraction. It can be seen from Equation 3.22 that, to a first approximation,

T_e is proportional to E/p. Noting that E is $(I/A)/\sigma$, an approximate scaling of the electron temperature is

$$\frac{(I/A)\,T_{t_0}}{\alpha p_{t_0} M_0^2}.$$

The dependencies on current and pressure are verified by Figs 3-5 and 3-6.

An important observation to be made is that, since the exit gas temperature depends only on M_0, and the frozen losses are found to correspond mostly to dissociation (which is governed by this temperature), these losses will become large below some critical value of the inlet Mach no. Figure 3-9 shows this to occur below $M_0 \approx 0.21$. It is also to be noted that, simultaneously, the channel is becoming excessively long ($L/D > 10$, probably leading to excessive viscous losses) as M_0 is reduced, and so is the electron temperature ($T_e \geq 7000$, probably initiating H_2 ionization). Increasing pressure can alleviate the rise in T_e (Fig. 3-4), but it also aggravates the L/D problem. On the other hand, reducing seed fraction (Figs 3-2 and 3-3) has the opposite effect of alleviating the L/D problem while elevating the electron temperature further. This combination of effects limits the specific impulse (Fig 3-9) to values not much higher than that for the baseline case.

Some sense of the two-dimensional degree of nonuniformity of the gas in the constrictor can be obtained from Figs. 3-10, 3-11 and 3-12, which show contours of v, T and T_e respectively for the nominal case; there is less constriction than in a conventional arcjet. Absent from the calculation are the wall boundary layers which would in actuality provide a thin transition to the wall temperature.

3.5 Summary and Conclusions

The results from this model suggest that cesium seeding of hydrogen arcjets is a feasible approach towards minimizing frozen losses efficiency, while maintaining an attractive specific impulse. At the same time, the generally reduced temperature levels should lead to fewer life time problems, and the presence of the easily ionizable alkali should also reduce near-electrode losses (although these aspects have not been analyzed).

Further increase in specific impulse is possible by raising the gas temperature, thus allowing more dissociation loss (but still avoiding the H ionization loss). However, operating the thruster at high temperatures might trigger ionization instability which could lead to a transition to a conventional hydrogen arc. There is a need to accurately model the physics

around the transition point. Quantitative treatment of this issue requires a more advanced approach beyond the quasi one dimensional model. This is the goal of the analysis carried out in the next chapter.

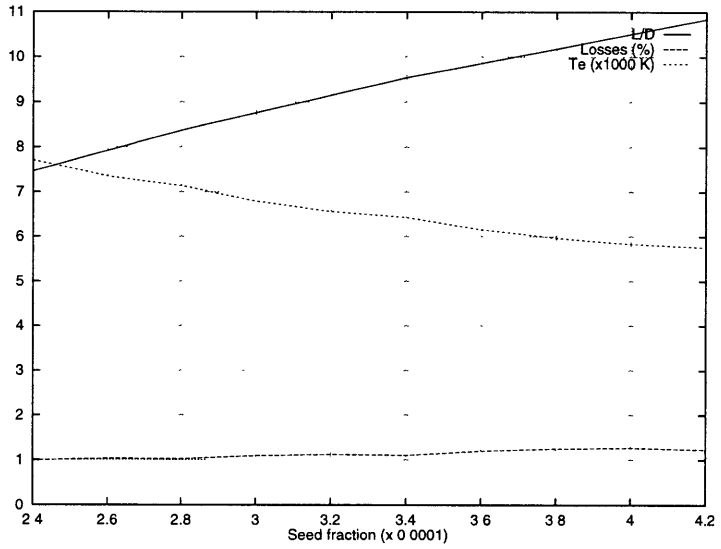

Figure 3-2: Exit electron temperature, L/D and frozen losses vs. seed fraction

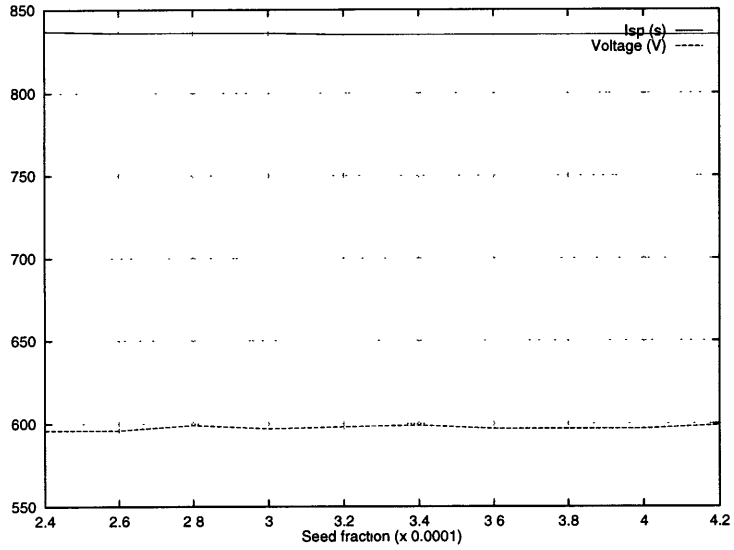

Figure 3-3: Specific impulse and arc voltage vs. seed fraction

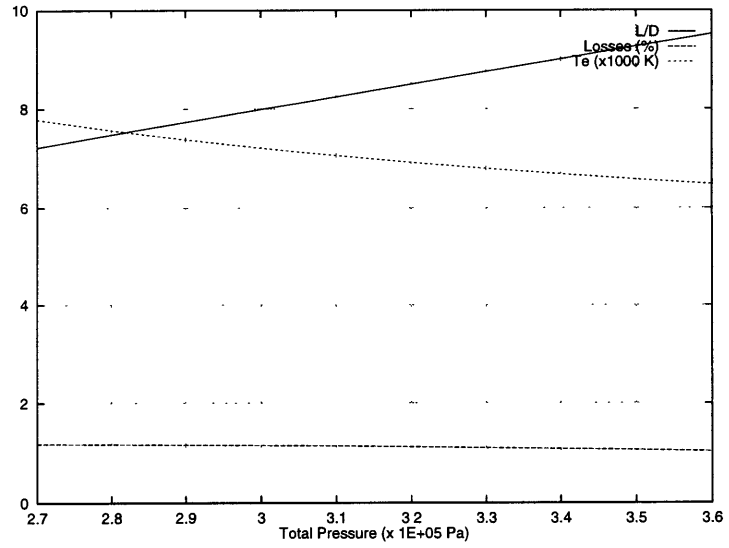

Figure 3-4: Exit electron temperature, L/D and frozen losses vs. total pressure

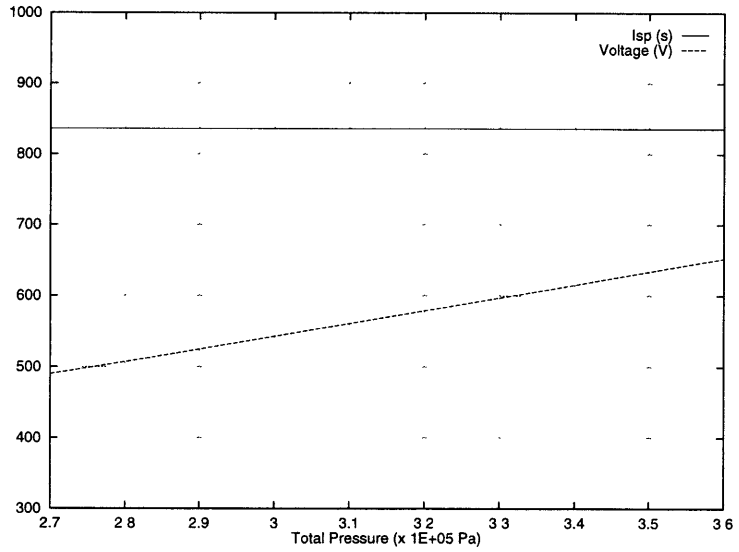

Figure 3-5: Specific impulse and arc voltage vs. total pressure

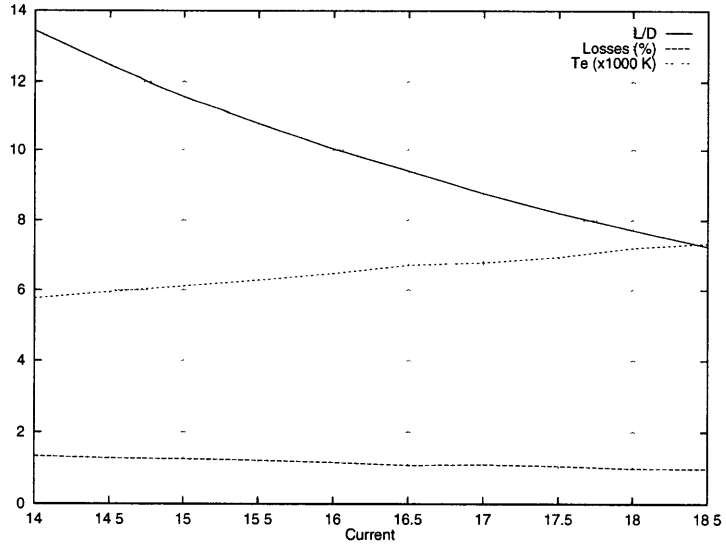

Figure 3-6: Exit electron temperature, L/D and frozen losses vs. current

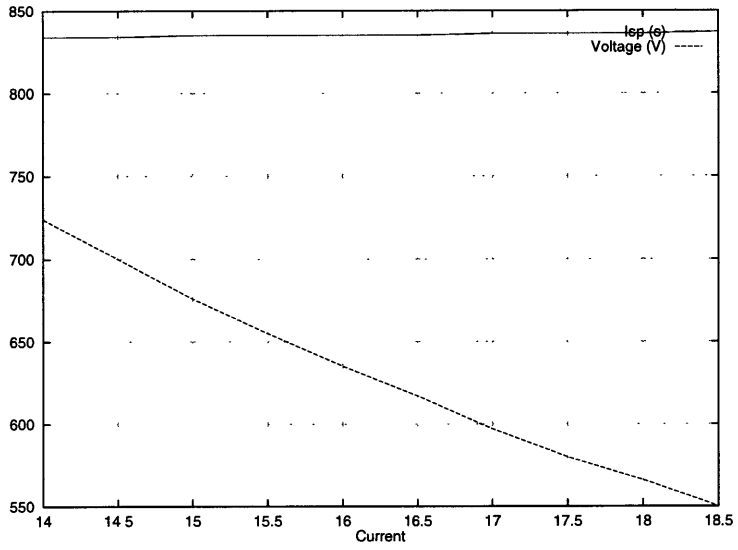

Figure 3-7: Specific impulse and arc voltage vs. current

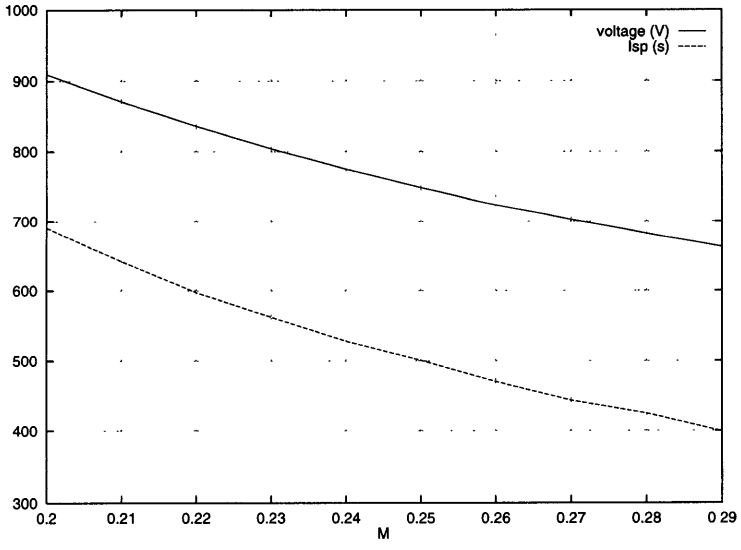

Figure 3-8: Specific impulse and arc voltage vs. inlet Mach number

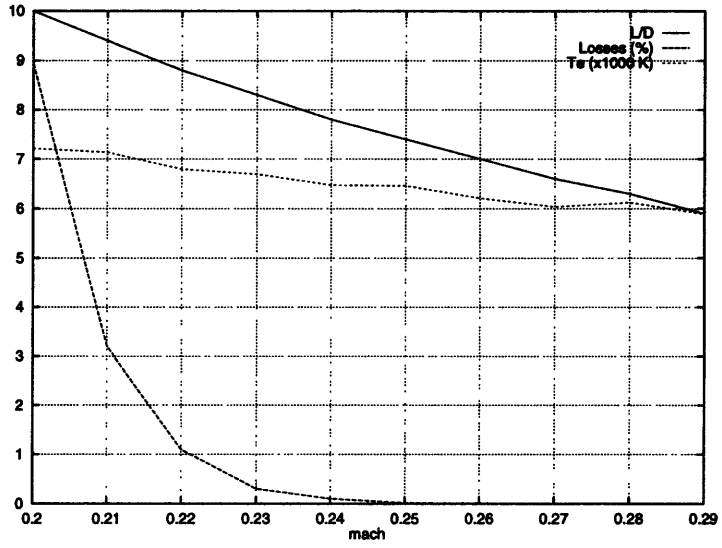

Figure 3-9: Exit electron temperature, L/D and frozen losses vs. inlet Mach number

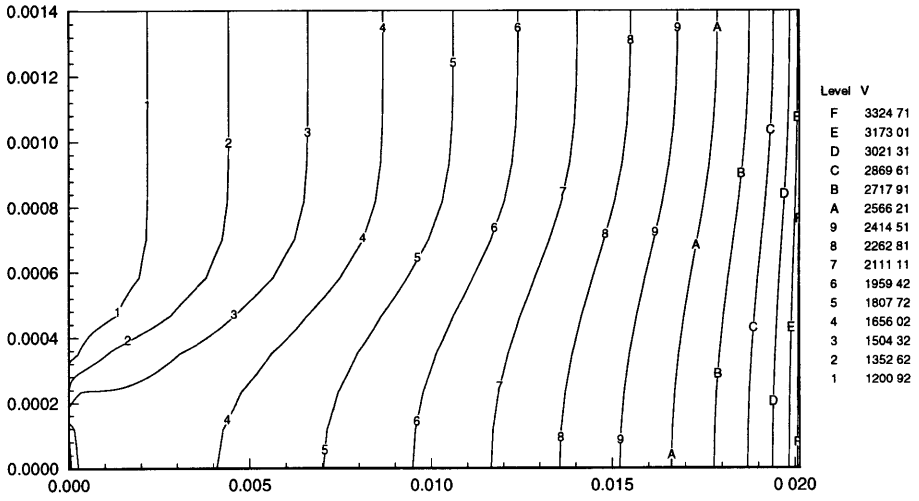

Figure 3-10: Gas velocity contour plot

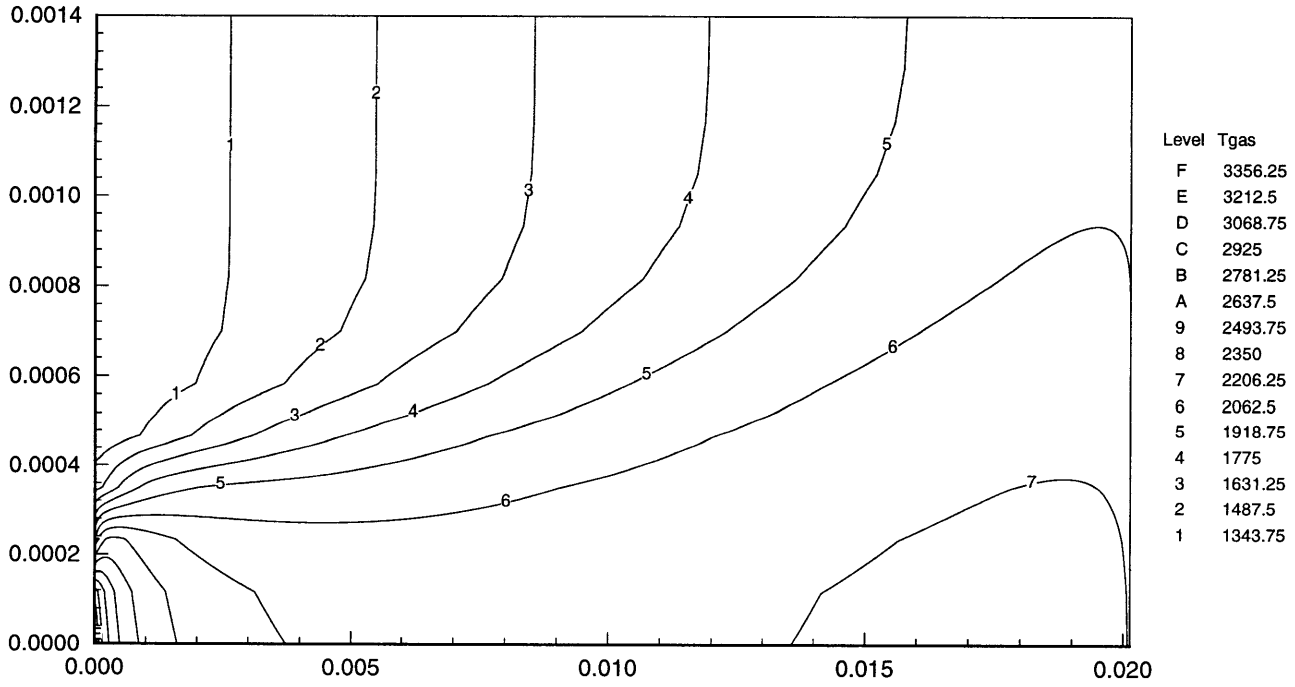

Figure 3-11: Gas temperature contour plot

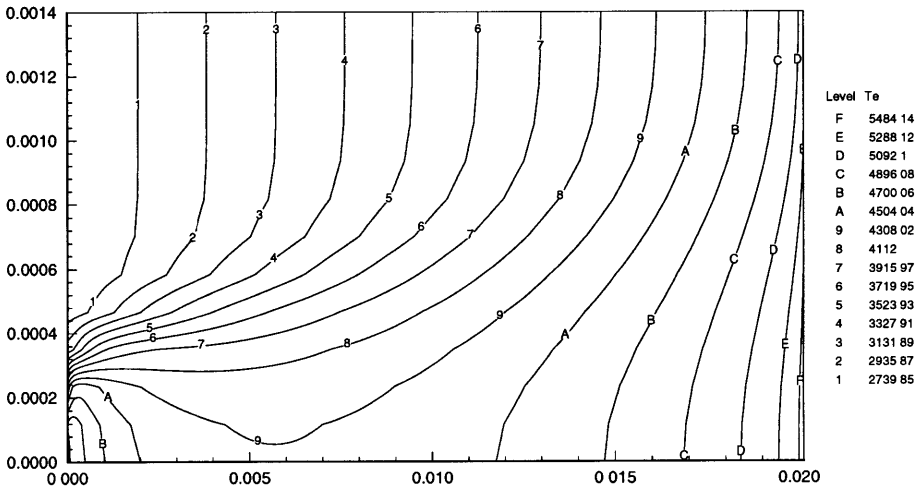

Figure 3-12: Electron temperature contour plot

Chapter 4

Stability Analysis

In the previous chapter, it was found that elimination of frozen losses in hydrogen arcjets via alkali seeding is indeed feasible. One of the draw backs to operating the device at lower temperature was found to be the corresponding decrease in specific impulse. A compromise that was proposed was to operate the device at higher gas temperature, thereby allowing a little bit of dissociation. However at higher degrees of dissociation, there is a concern that the maximum electron temperature restriction imposed in the previous analysis may no longer be valid, since the probability of electron impact ionization increases with greater atom concentration. A direct result of this is the possibility of ionization instabilities appearing in this regime. The presence of such instabilities could lead to a transition into conventional hydrogen arc. It is of primary importance, therefore, to probe the physics around this region. This is done, in this chapter, by performing a small perturbation analysis on the relevant governing equations.

4.1 Governing Equations

The species considered in the current model are H_2, H, H^+, C_s, C_s^+ and e. Unlike in the previous analysis, hydrogen dissociation and ionization are modeled in nonequilibrium via rate equations. The analysis is carried out in a semi-infinite channel of width W. For mathematical convenience, a Cartesian coordinate system is used. The flow velocity and global pressure are taken to be uniform; their perturbations also assumed negligible. As a result the global momentum equation reduces to the equation of state. For simplicity, cesium atoms and ions are modeled in Saha equilibrium with the electrons. Neglecting

convective terms, the effect of electron impact dissociation, energy invested in ionization and dissociation, and electron pressure gradients compared to Lorentz forces in the electron momentum equation, the relevant governing equations are

$$\frac{\partial n_{H^+}}{\partial t} = R n_e \left(S_H n_H - n_e n_{H^+} \right) \tag{4.1}$$

$$\frac{n_e n_{C_s^+}}{n_{C_s}} = S_{C_s}(T_e) \tag{4.2}$$

$$n_{C_s} + n_{C_s^+} = \alpha(2n_{H_2} + n_H + n_{H^+}). \tag{4.3}$$

$$n_e = n_{H^+} + n_{C_s^+} \tag{4.4}$$

$$\frac{\partial n_H}{\partial t} = K_f(T)\left(5n_H + 2n_{H_2}\right)\left(n_{H_2} - \frac{n_H^2}{K_n}\right) - R n_e \left(S n_e - n_e n_{H^+} \right) \tag{4.5}$$

$$\vec{j} = \sigma \vec{E} \tag{4.6}$$

$$p = \left(n_H + n_{H_2}\right) k_B T + n_e k_B \left(T_e + T\right) = const. \tag{4.7}$$

$$\frac{3}{2} n_e k_B \frac{\partial T_e}{\partial t} - \nabla \cdot \left(\kappa_e \nabla T_e\right) = \frac{j^2}{\sigma} - E_{coll} \tag{4.8}$$

$$\rho C_v \frac{\partial T}{\partial t} - \nabla \cdot \left(\kappa \nabla T\right) = E_{coll} \tag{4.9}$$

and

$$\nabla \cdot \left(\sigma \nabla \phi\right) = 0 \tag{4.10}$$

4.2 Linearization of the Governing Equations

The next step is to consider the response of the system to wave-like perturbations in densities, temperatures and electric potential of the form:

$$n_s = n_s^0 + \delta n_s \tag{4.11}$$

$$T_s = T_s^0 + \delta T_s \tag{4.12}$$

$$\phi = \phi^0 + \delta\phi \tag{4.13}$$

for all the species, s, present. The zero superscript denotes the steady state (zeroth order or background) values of the variables. The perturbations are assumed to be much smaller than the background, e.g.

$$\frac{\delta n_s}{n_s^0} \ll 1$$

The zero superscript is omitted hereafter. At steady state, the species conservation equations reduce to a system of nonlinear algebraic equations (equilibrium relations), which are solved simultaneously, to obtain the background densities from prescribed values of pressure, temperatures (T_e and T) and seed fraction:

$$\left(n_H + n_{H_2}\right) k_B T + n_e k_B \left(T_e + T\right) - p = 0, \tag{4.14}$$

$$n_H^2 - n_{H_2} K_n = 0, \tag{4.15}$$

$$\frac{n_e n_{H^+}}{n_H} - \left(\frac{2\pi m_e k T_e}{h^2}\right)^{\frac{3}{2}} e^{-\frac{\epsilon_{1H}}{kT_e}} = 0, \tag{4.16}$$

$$n_e - n_{C_s^+} - n_{H^+} = 0, \tag{4.17}$$

$$\frac{n_e n_{C_s^+}}{n_{C_s}} = S_{C_s}(T_e) \tag{4.18}$$

and

$$n_{C_s^+} + n_{C_s} - \alpha\left(n_{H^+} + n_H + 2n_{H_2}\right) = 0, \tag{4.19}$$

The background current density is then calculated from the electron energy balance at steady state:

$$j = \sqrt{\sigma E_{coll}} \tag{4.20}$$

Substitution of the new expressions for densities, temperatures and potential into the governing equations, after linearization, leads to expressions for the perturbed governing

equations:

$$\delta n_e - \delta n_{H^+} - \delta n_{C_s^+} = 0 \tag{4.21}$$

$$\frac{\partial}{\partial t}(\delta n_{H^+}) = \delta \dot{n}_{H^+} \tag{4.22}$$

$$n_{C_s^+}\delta n_e + n_e \delta n_{C_s^+} = S_{cs}\left[\delta n_{C_s} + n_{C_s}\left(\frac{\epsilon_{i_{C_s}}}{k_B T_e^2} + \frac{3}{2T_e}\right)\delta T_e\right] \tag{4.23}$$

$$\frac{\partial}{\partial t}(\delta n_H) = -\delta \dot{n}_{H_2} - \delta \dot{n}_{H^+} \tag{4.24}$$

$$\delta n_{C_s} + \delta n_{C_s^+} = \alpha\left(\delta n_{H^+} + \delta n_H + 2\delta n_{H_2}\right) \tag{4.25}$$

$$\left(\frac{T_e}{T} + 1\right)\delta n_e + \delta n_H + \delta n_{H_2} + \left(\frac{n_e}{T}\right)\delta T_e + \left(\frac{n_e + n_H + n_{H_2}}{T}\right)\delta T = 0 \tag{4.26}$$

$$\frac{3}{2} n_e k_B \frac{\partial}{\partial t}(\delta T_e) - \kappa_e \nabla^2(\delta T_e) = -2j\frac{\partial \delta\phi}{\partial x} + \delta\sigma\frac{j^2}{\sigma} - \delta E_{coll} \tag{4.27}$$

$$\rho C_v \frac{\partial}{\partial t}(\delta T) - \kappa \nabla^2(\delta T) = \delta E_{coll} \tag{4.28}$$

and

$$\nabla^2 \delta\phi - \frac{j}{\sigma^2}\frac{\partial}{\partial x}(\delta\sigma) = 0 \tag{4.29}$$

where perturbations in production rates, electrical conductivity, and collisional energy transfer are

$$\begin{aligned}\delta \dot{n}_{H^+} = &-(R_{Sh} n_e n_{H^+})\delta n_e - (R_{Sh} n_e^2)\delta n_{H^+} + (R_{Sh} n_e S_H)\delta n_H \\ &+ \left[R_{Sh} n_e n_H S_H\left(\frac{\epsilon_{i_H}}{k_B T_e^2} + \frac{3}{2T_e}\right)\right]\delta T_e\end{aligned} \tag{4.30}$$

$$\delta\dot{n}_{H_2} = -K_f\left(5n_H + 2n_{H_2}\right)\left[-2\left(\frac{n_H}{K_n}\right)\delta n_H + \delta n_{H2} + n_{H_2}\left(\frac{1}{2T} + \frac{\theta_d}{T^2} - \frac{\theta_v}{T^2}\frac{1}{exp\left(\theta_v/T\right)-1}\right)\delta T\right] \tag{4.31}$$

$$\delta\sigma = \sigma\left[\left(1 - \frac{\nu_{ei}}{\nu_e}\right)\frac{\delta n_e}{n_e} - \frac{\nu_{eH}}{\nu_e}\frac{\delta n_H}{n_H} - \frac{\nu_{eH_2}}{\nu_e}\frac{\delta n_{H_2}}{n_{H_2}} - \left(\frac{1}{\nu_e}\frac{\partial\nu_e}{\partial T_e}\right)\delta T_e\right] \tag{4.32}$$

$$\delta E_{coll} = E_{coll}\left[\left(1 + \frac{\nu_{ei}}{nu_e^*}\right)\frac{\delta n_e}{n_e} + \frac{\nu_{eH}}{nu_e^*}\frac{\delta n_H}{n_H} + \frac{\nu_{eH_2}\delta_{H_2}}{2nu_e^*}\frac{\delta n_{H_2}}{n_{H_2}} + \left(\frac{1}{\nu_e^*}\frac{\partial\nu_e^*}{\partial T_e} + \frac{1}{(T_e - T)} +\right)\delta T_e - \frac{\delta T}{T_e - T}\right] \tag{4.33}$$

Here

$$\nu_e^* \equiv \nu_{eH} + \nu_{ei} + \frac{\nu_{eH_2}}{2}\delta_{n_{H_2}} \tag{4.34}$$

The derivatives $\frac{\partial\nu_e}{\partial T_e}$ and $\frac{\partial\nu_e^*}{\partial T_e}$ are evaluated numerically.

Nondimensional Groups

For ease of analysis, the following group of nondimensional parameters are introduced:

$$\tau = \frac{t}{t_D} \tag{4.35}$$

$$\hat{x} = \frac{x}{L_D} \tag{4.36}$$

$$\hat{y} = \frac{y}{L_D} \tag{4.37}$$

$$\tilde{n}_s = \frac{\delta n_s}{n_s} \tag{4.38}$$

$$\tilde{T}_s = \frac{\delta T_s}{T_s} \tag{4.39}$$

$$\tilde{\phi} = \frac{\delta\phi}{\phi} \tag{4.40}$$

$$\Theta = \frac{T_e}{T} \tag{4.41}$$

$$\Upsilon = \frac{C_p}{C_v} \tag{4.42}$$

$$\Omega = \left(\frac{\epsilon_{i_H}}{k_B T_e} + \frac{3}{2}\right) \tag{4.43}$$

$$G = \left(\frac{\epsilon_{i_{C_s}}}{k_B T_e} + \frac{3}{2}\right) \tag{4.44}$$

$$\Gamma = \left(\frac{1}{2T} + \frac{\theta_d}{T^2} - \frac{\theta_v}{T^2}\frac{1}{e^{\left(\frac{\theta_v}{T}\right)} - 1}\right) \tag{4.45}$$

$$\hat{R}_i = R_{Sh} n_H S_H t_D \tag{4.46}$$

$$\hat{R}_d = \frac{K_f \left(5n_H + 2n_{H_2}\right) n_H t_D}{K_n} \tag{4.47}$$

$$D_g = \frac{\kappa t_D}{\rho C_v L^2} \tag{4.48}$$

$$\Lambda = \frac{E_{coll} t_D}{\rho C_v T} \tag{4.49}$$

$$\Xi = \frac{\epsilon_d n_H}{\rho C_v T} \tag{4.50}$$

$$C = \frac{T_e}{\nu_e}\frac{\partial \nu_e}{\partial T_e} \tag{4.51}$$

$$C^* = \frac{T_e}{\nu_e^*}\frac{\partial \nu_e^*}{\partial T_e} \tag{4.52}$$

where the diffusive length and time scales are defined respectively as

$$t_D = \left(\frac{\frac{3}{2} n_e k_B T_e \sigma}{j^2}\right) \tag{4.53}$$

$$L_D = \sqrt{\frac{\kappa_e t_D}{\frac{3}{2} n_e K_B}} \tag{4.54}$$

The reference potential is arbitrarily chosen to be

$$\phi = \frac{j L_D}{\sigma} \tag{4.55}$$

As a result, the linearized perturbation equations can now be expressed in the form:

$$\left(1 + \frac{n_{C_s^+}}{n_e + S_{C_s}}\right)\tilde{n}_e - \frac{n_{H^+}}{n_e}\tilde{n}_{H^+} - \frac{n_{C_s^+}}{n_e(2n_{H_2} + n_H)}\left(n_H \tilde{n}_H + 2n_{H_2}\tilde{n}_{H_2}\right) - \frac{n_{C_s^+}}{n_e} G \left(1 - \frac{n_{C_s^+}}{\alpha(2n_{H_2} + n_H)}\right)\tilde{T}_e \tag{4.56}$$

$$\frac{\partial \tilde{n}_{H^+}}{\partial \tau} = \hat{R}_i \left(-\tilde{n}_e - \tilde{n}_{H^+} + \tilde{n}_H + \Omega \tilde{T}_e\right) \tag{4.57}$$

$$\frac{\partial \tilde{n}_H}{\partial \tau} = \hat{R}_i \frac{n_{H^+}}{n_H}\left(\tilde{n}_e + \tilde{n}_{H^+} - \Omega \tilde{T}_e\right) - \left(2\hat{R}_d + \hat{R}_i \frac{n_{H^+}}{n_H}\right)\tilde{n}_H + \hat{R}_d\left(\tilde{n}_{H_2} + \Gamma \tilde{T}\right) \tag{4.58}$$

$$\frac{n_e}{n_{H_2}}(\Theta + 1)\,\tilde{n}_e + \frac{n_H}{n_{H_2}}\tilde{n}_H + \tilde{n}_{H_2} + \frac{n_e}{n_{H_2}}\Theta \tilde{T}_e + \frac{n_e + n_H + n_{H_2}}{n_{H_2}}\tilde{T} = 0 \tag{4.59}$$

$$\frac{\partial \tilde{T}_e}{\partial \tau} - \hat{\nabla}^2 \tilde{T}_e = -\left(\frac{\nu_{ei}}{\nu_e} + \frac{\nu_{ei}}{\nu_e^*}\right)\tilde{n}_e - \left(\frac{\nu_{eH}}{\nu_e} + \frac{\nu_{eH}}{\nu_e^*}\right)\tilde{n}_H - \left(\frac{\nu_{eH_2}}{\nu_e} + \frac{\nu_{eH_2}}{\nu_e^*}\right)\tilde{n}_{H_2} + \left(C + \frac{\Theta}{\Theta - 1} + C^*\right)\tilde{T}_e \frac{\tilde{T}}{\Theta - 1} - 2\frac{\partial \tilde{\phi}}{\partial \hat{x}} \tag{4.60}$$

$$\frac{\partial \tilde{T}}{\partial \tau} - D_g \hat{\nabla}^2 \tilde{T} = \Lambda\left[\left(1 + \frac{\nu_{ei}}{\nu_e^*}\right)\tilde{n}_e + \frac{\nu_{eH}}{\nu_e^*}\tilde{n}_H + \frac{\delta_{H_2}}{2}\frac{\nu_{eH_2}}{\nu_e^*}\tilde{n}_{H_2} + \left(\frac{\Theta}{\Theta - 1} + C^*\right)\tilde{T}_e - \frac{\tilde{T}}{\Theta - 1}\right] \tag{4.61}$$

$$\hat{\nabla}^2 \tilde{\phi} - \left(1 - \frac{\nu_{ei}}{\nu_e}\right)\frac{\partial \tilde{n}_e}{\partial \hat{x}} - \frac{\nu_H}{\nu_e}\frac{\partial \tilde{n}_H}{\partial \hat{x}} - \frac{\nu_{H_2}}{\nu_e}\frac{\partial \tilde{n}_{H_2}}{\partial \hat{x}} - C\frac{\partial \tilde{T}_e}{\partial \hat{x}} \tag{4.62}$$

where we have substituted for $\delta n_{C_s^+}$ and δn_{C_s} using Equations 4.23 and 4.25.

4.3 Dispersion Relations

As is usual in linear stability analysis, the disturbance is now decomposed into its Fourier components:

$$\tilde{n}_s = \hat{n}_s\, e^{i(\vec{k}\cdot\vec{r} - \omega\tau)} \tag{4.63}$$

$$\tilde{T}_s = \hat{T}_s\, e^{i(\vec{k}\cdot\vec{r} - \omega\tau)} \tag{4.64}$$

$$\tilde{\phi} = \hat{\phi}\, e^{i(\vec{k}\cdot\vec{r} - \omega\tau)} \tag{4.65}$$

where the hatted quantities are the complex amplitudes, $\vec{k}$ and $\vec{r}$ are the wave and radius vectors respectively. The quantity ω is the complex frequency:

$$\omega = \omega_r + i\,\omega_i \tag{4.66}$$

The wave vector is set to lie at angle θ with the background current (x-axis), so that

$$\vec{k} \cdot \vec{r} = k\,(\hat{x}\,cos\,\theta + \hat{y}\,sin\,\theta) \tag{4.67}$$

As a result,

$$\frac{\partial}{\partial t} \rightarrow -i\omega \tag{4.68}$$

$$\frac{\partial}{\partial x} \rightarrow ik\,cos\,\theta \tag{4.69}$$

$$\frac{\partial}{\partial y} \rightarrow ik\,sin\,\theta \tag{4.70}$$

$$\nabla^2 \rightarrow -k^2 \tag{4.71}$$

After Fourier decomposition, the linearized perturbation equations reduce to a system of algebraic equation which can be expressed in matrix form as

$$\begin{pmatrix} A_{11}\,A_{12}\,A_{13}\,A_{14}\,A_{15}\,A_{16}\,A_{17} \\ A_{21}\,A_{22}\,A_{23}\,A_{24}\,A_{25}\,A_{26}\,A_{27} \\ A_{31}\,A_{32}\,A_{33}\,A_{34}\,A_{35}\,A_{36}\,A_{37} \\ A_{41}\,A_{42}\,A_{43}\,A_{44}\,A_{45}\,A_{46}\,A_{47} \\ A_{51}\,A_{52}\,A_{53}\,A_{54}\,A_{55}\,A_{56}\,A_{57} \\ A_{61}\,A_{62}\,A_{63}\,A_{64}\,A_{65}\,A_{66}\,A_{67} \\ A_{71}\,A_{72}\,A_{73}\,A_{74}\,A_{75}\,A_{76}\,A_{77} \end{pmatrix} \begin{pmatrix} \tilde{n}_e \\ \tilde{n}_{H^+} \\ \tilde{n}_H \\ \tilde{n}_{H_2} \\ \tilde{T}_e \\ \tilde{T} \\ \tilde{\phi} \end{pmatrix} = 0 \tag{4.72}$$

where the coefficients of the matrix, A, are

$$A_{11} = \left(1 + \frac{n_{C_s^+}}{n_e + S_{C_s}}\right) \tag{4.73}$$

$$A_{12} = -\frac{n_{H^+}}{n_e} \tag{4.74}$$

$$A_{13} = -\frac{n_H n_{C_s^+}}{n_e(2n_{H_2} + n_H)} \tag{4.75}$$

$$A_{14} = -\frac{2n_{H_2} n_{C_s^+}}{n_e(2n_{H_2} + n_H)} \tag{4.76}$$

$$A_{15} = -\frac{n_{C_s^+}}{n_e} G \left(1 - \frac{n_{C_s^+}}{\alpha(2n_{H_2} + n_H)}\right) \tag{4.77}$$

$$A_{16} = 0 \tag{4.78}$$

$$A_{17} = 0 \tag{4.79}$$

$$A_{21} = -\hat{R}_i \tag{4.80}$$

$$A_{22} = i\omega - \hat{R}_i \tag{4.81}$$

$$A_{23} = \hat{R}_i \tag{4.82}$$

$$A_{24} = 0 \tag{4.83}$$

$$A_{25} = \hat{R}_i \Omega \tag{4.84}$$

$$A_{26} = 0 \tag{4.85}$$

$$A_{27} = 0 \tag{4.86}$$

$$A_{31} = \hat{R}_i \frac{n_{H^+}}{n_H} \tag{4.87}$$

$$A_{32} = \hat{R}_i \frac{n_{H^+}}{n_H} \tag{4.88}$$

$$A_{33} = i\omega - 2(\hat{R}_d - \hat{R}_i \frac{n_{H^+}}{n_H}) \tag{4.89}$$

$$A_{34} = \hat{R}_d \tag{4.90}$$

$$A_{35} = -\hat{R}_i \frac{n_{H^+}}{n_H} \Omega \tag{4.91}$$

$$A_{36} = \hat{R}_d \Gamma \tag{4.92}$$

$$A_{37} = 0 \tag{4.93}$$

$$A_{41} = \frac{n_e}{n_{H_2}} (\Theta + 1) \tag{4.94}$$

$$A_{42} = 0 \tag{4.95}$$

$$A_{43} = \frac{n_H}{n_{H_2}} \tag{4.96}$$

$$A_{44} = 1 \tag{4.97}$$

$$A_{45} = \frac{n_e}{n_{H_2}} \Theta \tag{4.98}$$

$$A_{46} = \frac{n_e + n_H + n_{H_2}}{n_{H_2}} \tag{4.99}$$

$$A_{47} = 0 \tag{4.100}$$

$$A_{51} = -\left(\frac{\nu_{ei}}{\nu_e} + \frac{\nu_{ei}}{\nu_e^*}\right) \tag{4.101}$$

$$A_{52} = 0 \tag{4.102}$$

$$A_{53} = -\left(\frac{\nu_{eH}}{\nu_e} + \frac{\nu_{eH}}{\nu_e^*}\right) \tag{4.103}$$

$$A_{54} = -\left(\frac{\nu_{eH_2}}{\nu_e} + \frac{\nu_{eH_2}}{\nu_e^*}\right) \tag{4.104}$$

$$A_{55} = i\omega - k^2 - \left(C + \frac{\Theta}{\Theta - 1} + C^*\right) \tag{4.105}$$

$$A_{56} = \frac{1}{\Theta - 1} \tag{4.106}$$

$$A_{57} = -i2k\cos(\theta) \tag{4.107}$$

$$A_{61} = \Lambda\left(1+\frac{\nu_{ei}}{\nu_e^*}\right) \tag{4.108}$$

$$A_{62} = 0 \tag{4.109}$$

$$A_{63} = \Lambda\frac{\nu_{eH}}{\nu_e^*} \tag{4.110}$$

$$A_{64} = \Lambda\frac{\delta_{H_2}}{2}\frac{\nu_{eH_2}}{\nu_e^*} \tag{4.111}$$

$$A_{65} = \Lambda\left(\frac{\Theta}{\Theta-1}+C^*\right) \tag{4.112}$$

$$A_{66} = i\omega - D_g k^2 - \frac{\Lambda}{\Theta-1} \tag{4.113}$$

$$A_{67} = 0 \tag{4.114}$$

$$A_{71} = -\left(1-\frac{\nu_{ei}}{\nu_e}\right)ik\cos\theta \tag{4.115}$$

$$A_{72} = 0 \tag{4.116}$$

$$A_{73} = \frac{\nu_H}{\nu_e}ik\cos\theta \tag{4.117}$$

$$A_{74} = \frac{\nu_{H_2}}{\nu_e}ik\cos\theta \tag{4.118}$$

$$A_{75} = ikC\cos\theta \tag{4.119}$$

$$A_{76} = 0 \tag{4.120}$$

$$A_{77} = -k^2 \tag{4.121}$$

The dispersion relation is then obtained by setting the determinant of matrix A to zero:

$$F(w,k,\theta,T_e,\alpha,T,p) = det[A] = 0 \tag{4.122}$$

The resulting expression for F is very complicated. It can, however, be written in the form:

$$F = k^2\left[f_1(w,k) + \cos^2(\theta)\, f_2(w,k)\right] \tag{4.123}$$

where f_1 is a polynomial of degree 4 in both ω and k, and f_2 is of second degree in both k and ω. The roots of equation 4.122 represent the different modes of propagation of the disturbance. The sign of ω_i indicates the development of the perturbation in time: positive signifies growth, hence instability, while negative indicates a decaying stable mode. The general requirement of system stability is for all ω_i to be negative ($\omega_i = 0$ signifies marginal stability). From mathematical analysis, the magnitude and orientation of the wave vector

at extrema of the function $\omega_i = \omega_i(k, \theta)$ are obtained from the conditions:

$$\Im\left(\frac{\partial \omega}{\partial k}\right) = 0 \tag{4.124}$$

and

$$\Im\left(\frac{\partial \omega}{\partial \theta}\right) = 0 \tag{4.125}$$

where $\Im$ denotes imaginary part of the expression. Unfortunately an analytical expression for $\omega_i(k, \theta)$ is not possible. However, the above expression can be rearranged in the form:

$$\Im\left(\frac{\partial F}{\partial k} / \frac{\partial F}{\partial \omega}\right) = 0 \tag{4.126}$$

and

$$\Im\left(\frac{\partial F}{\partial \theta} / \frac{\partial F}{\partial \omega}\right) = 0 \tag{4.127}$$

A close inspection of Equation 4.123 shows that these conditions are satisfied by

$$k = 0 \tag{4.128}$$

$$sin\,\theta\, cos\,\theta = 0 \tag{4.129}$$

This result is supported by Figure 4-1, which shows the variation of ω_i with θ at different values of k for background values: $T = 3000K$, $T_e = 8000K$, $p = 1atm$ and $\alpha = 10^{-4}$, where it can be seen that $k = 0$ and $\theta = \frac{\pi}{2}$ ($cos\,\theta$=0) correspond to the least stable mode, while $\theta = 0$ ($sin\,\theta$=0) is the most stable mode. Hence, it can be concluded that the least stable mode occurs at an angle $\frac{\pi}{2}$ between the wave vector and background current density, and at the maximum possible wavelength of propagation, which in this case equals twice the channel width.

4.4 Results

In this section, the behavior of the system on variation of each of the background parameters is discussed. The analysis is confined to the wave vector corresponding to the least stable mode ($k = 0$ and $\theta = \frac{\pi}{2}$).

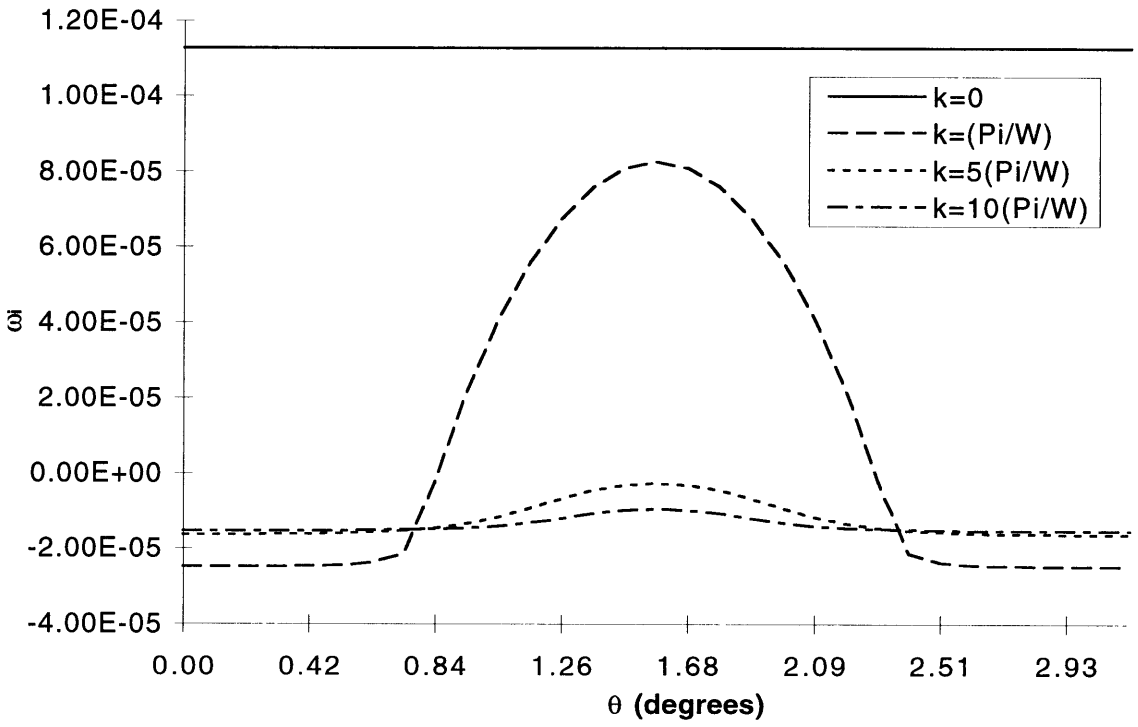

Figure 4-1: Nondimensional Imaginary Frequency versus wave vector

4.4.1 Stability Behavior as a Function of Electron Temperature

Figure 4-2 shows the variation of the imaginary frequency of the least stable mode with electron temperature for $T = 2000K$, $P = 1atm$ and $\alpha = 10^{-4}$. It can be inferred from the plot, that there are two regimes of instability: $T_{e_I} < 5630$ and $T_{e_{II}} > 8380$. These instabilities are ionizational (or electrothermal) in nature. An ionization instability occurs in regions of localized increase in electrical conductivity generally caused by fluctuations in densities and temperatures. Accompanying this, is an increase in Joule dissipation, due to current concentration in this region, which in turn fuels the electron temperature increase; hence, an instability ensues. This is confirmed in Figure 4-3 which shows $\tilde{\sigma}$ (normalized against $\tilde{T}_e$) versus electron temperature.

In order to understand the mechanisms of these instabilities, consider a positive fluctuation in electron temperature ($\tilde{T}_e > 0$). From the gas temperature perturbation equation, it can be seen that a positive fluctuation in electron temperature would lead to a corresponding increase in the gas temperature, hence, a negative perturbation in the overall density (from equation of state at constant pressure). This fluctuation in electron temperature will also favor the ionization process in regions where the seed is not fully ionized. The direction of electron density perturbation therefore depends on which the two effects (expansion and ionization) is stronger: positive in regions of strong ionization ($T_e \ll T_{e_I}$), and negative near the threshold, T_{e_I}. At low electron temperatures, Coulombic interactions tend to dominate because of the large electron ion collision cross section. Because the Coulomb collision frequency is inversely proportional to T_e, its partial derivative with electron temperature will be negative in this region, hence the nondimensional parameter $C < 0$. From Equation 4.32, it can be seen that the combination of these two effects at low T_e will lead to a positive fluctuation in conductivity, causing the system to go unstable. This trend continues until near full seed ionization where $\tilde{n}_e$ becomes negative. This coupled with the corresponding decrease in Coulombic interactions would result in stability being restored to the system. This argument is supported by Figure 4-4 which shows the variation of $\tilde{n}_e$ and C with temperature around the transition region.

As mentioned earlier, the perturbation in temperature of the gas goes in the same direction as that of the electron. If the gas temperature is high enough, this positive fluctuation in gas temperature would favor the dissociation process, so that $\tilde{n}_{H_2} < 0$ and

$\tilde{n}_H > 0$ (in the absence of H ionization). However, as the electron temperature approaches $T_{e_{II}}$, $\tilde{n}_H$ decreases, because of the ionization process, and becomes negative at $T_e > T_{e_{II}}$. Figure 4-5 shows the variation of $\tilde{n}_H$ (normalized against $\tilde{T}_e$) with temperature in this region. As can be seen from Equation 4.32, this effect coupled with increase in $\tilde{n}_e$ would result in increase in conductivity.

4.4.2 Stability Behavior as a Function of Gas Temperature and Pressure

Illustrated in Figure 4-6 is a plot of background values of electron temperature against gas temperature at different pressures near the stability threshold. The lower plots represent the conditions below which the seed ionization instability occurs (mode I), while the second group corresponds to conditions above which hydrogen ionization instability occurs (mode II). It can be seen from the plots that the electron temperature at which instabilities occur decreases with an increase in gas temperature. This is so, because an increase in dissociation occurs as temperature increases, hence there are more atoms of hydrogen present for the electrons to ionize. An important observation made in the region of H ionization instability is that they typically occur when electrons from hydrogen atoms constitute about 2% of total. As seen from the plot, an increase in pressure delays the temperature at which the instabilities occur.

4.4.3 Stability Behavior as a Function of Cesium Seed Fraction

As mentioned earlier, the primary driving force for the first instability mode is due to dominance of Coulombic interaction in this region. As a result, we expect this effect to disappear at conditions where the coulombic interactions are not important. A comparison of the Coulomb collision frequency to that of $e - H_2$ shows that an approximate threshold condition is when

$$\frac{\nu_{ei}}{\nu_{eH}} \approx \frac{1.17 \times 10^{-9} \alpha ln\Lambda}{Q_{eH_2}(T_e)} \ll 1 \tag{4.130}$$

From the above expression, we can estimate the electron temperatures below which seed ionization instability occurs for a given seed fraction, and vice versa. Some numerical examples are based on this estimation are displayed in Table 4.1. These results are approximately confirmed by the lower plot in Figure 4-7 which shows the dependence of electron temperature on seed fraction at stability threshold ($p = 1atm.$ and $T = 2000K$). The upper plot

Table 4.1: Approximate values of electron temperature below which seed ionization instability occurs for a given seed fraction

α	T_e
10^{-4}	2936
3×10^{-4}	4707
5×10^{-4}	5821
10^{-3}	7710
1.2×10^{-3}	8291

shows the dependence of $T_{e_{II}}$ versus the seed fraction. The reason why the $T_{e_{II}}$ decreases with a corresponding decrease in seed fraction has to do with the increase in the proportion of electrons from atomic hydrogen with a decrease in seed fraction. It can be noticed, however, that the two temperatures, i.e T_{e_I} and $T_{e_{II}}$ approach each other at high seed fraction. The value at which this occur is the upper bound on seed fraction, and results in a situation where the system is always unstable.

4.5 Summary and Conclusions

The results from this analysis confirm our intuition about possible ionization instabilities in the system. It was found that there are two regimes in which these instabilities occur. The first regime, due to seed ionization, was found to occur at electron temperatures where the seed is not fully ionized, and where Coulombic interactions are relevant. It was also found that decreasing the seed fraction essentially reduces the temperatures at which this instability occurs. However, due to the requirement for conductivity, such an approach for curbing the instability is not practical. Furthermore, since this instability disappears after full ionization of the seed, its direct effect will be simply to drive the electron temperature above its threshold values to nearly full ionization of the seed. This will occur in the "core" of the arc, which according to the nonlinear calculations of the previous chapter, is not strongly constricted in any case.

Of major concern, however, is the second regime which corresponds to hydrogen ionization instability. It was found that this instability occurs at temperatures above the range investigated in the analysis of the previous chapter. Hence, we conclude that our previous analysis is valid. The electron temperatures at which this instability occur was found to

be strongly dependent on degrees of dissociation and ionization. As a result, operating the device at higher gas temperatures, hence higher specific impulse, reduces the maximum allowable electron temperature.

Absent from the analysis are the effects of electron diffusion, radiation and convection which otherwise would help in damping out the instabilities.

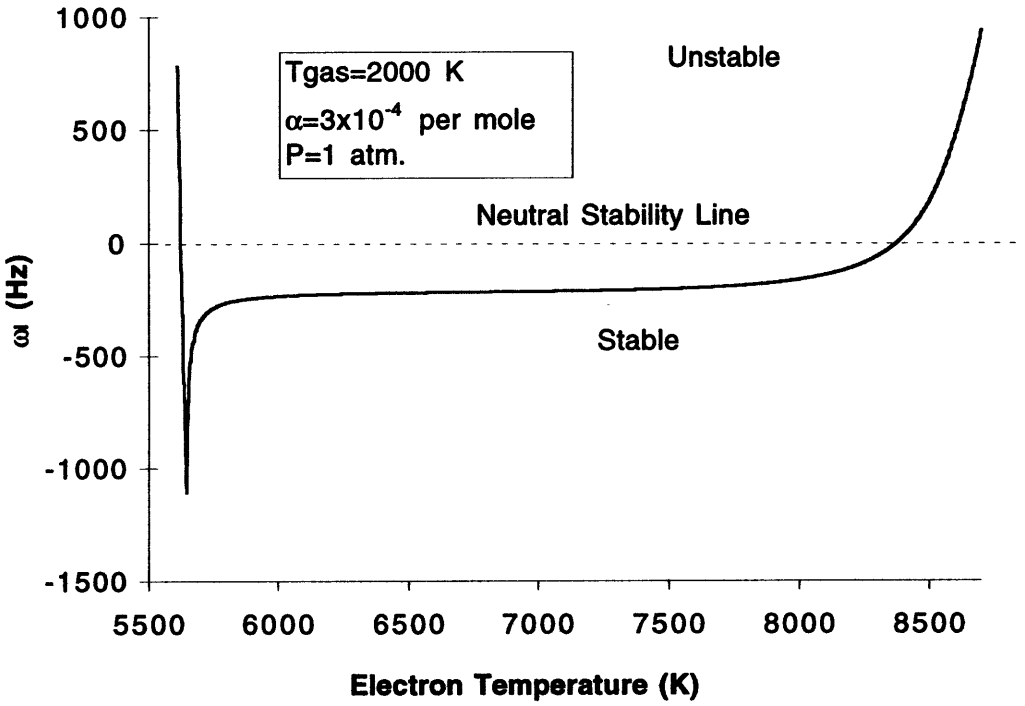

Figure 4-2: Imaginary frequency vs electron temperature

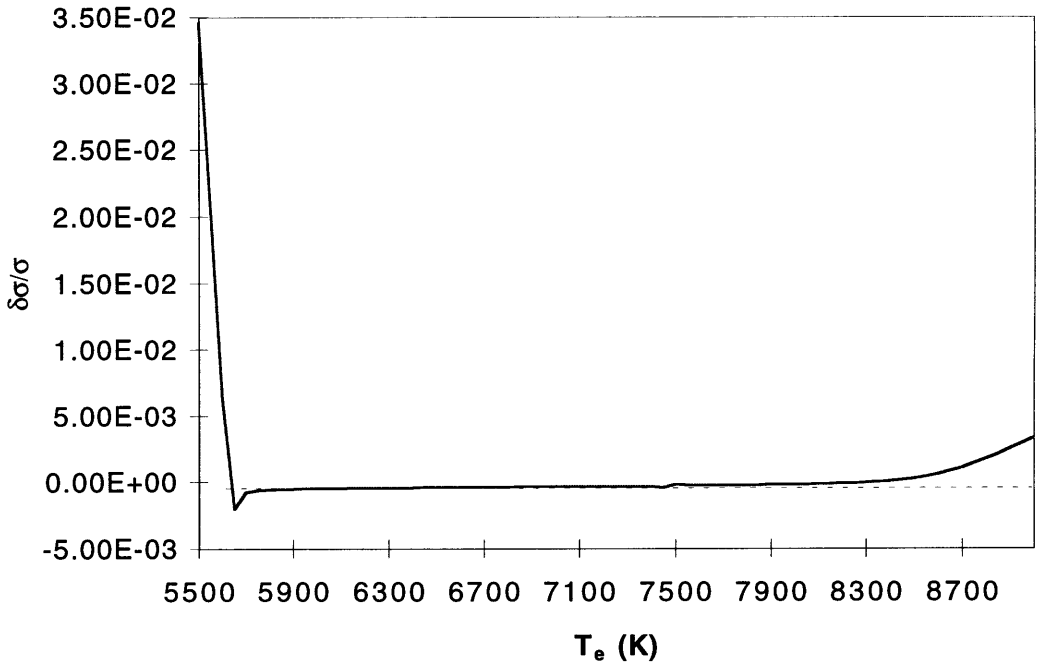

Figure 4-3: Relative perturbation in conductivity versus electron temperature

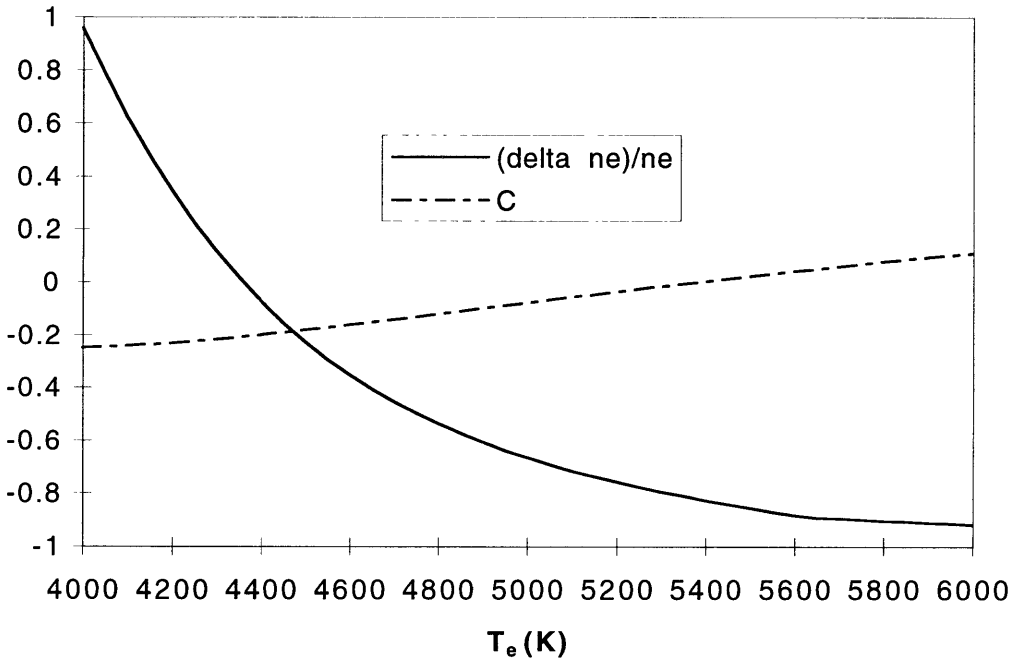

Figure 4-4: Electron density perturbation and nondimensional parameter C versus electron temperature

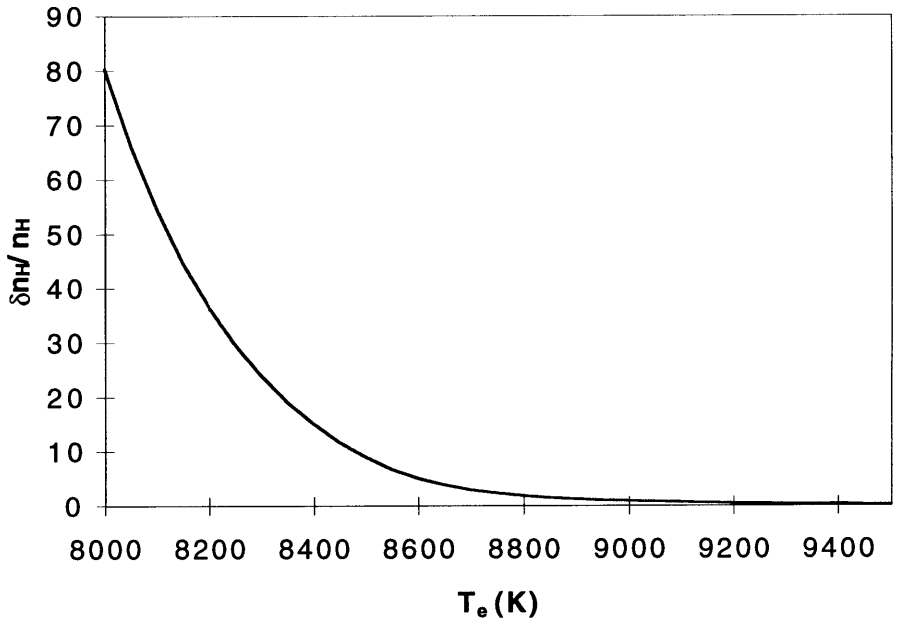

Figure 4-5: Atomic hydrogen density perturbation versus electron temperature

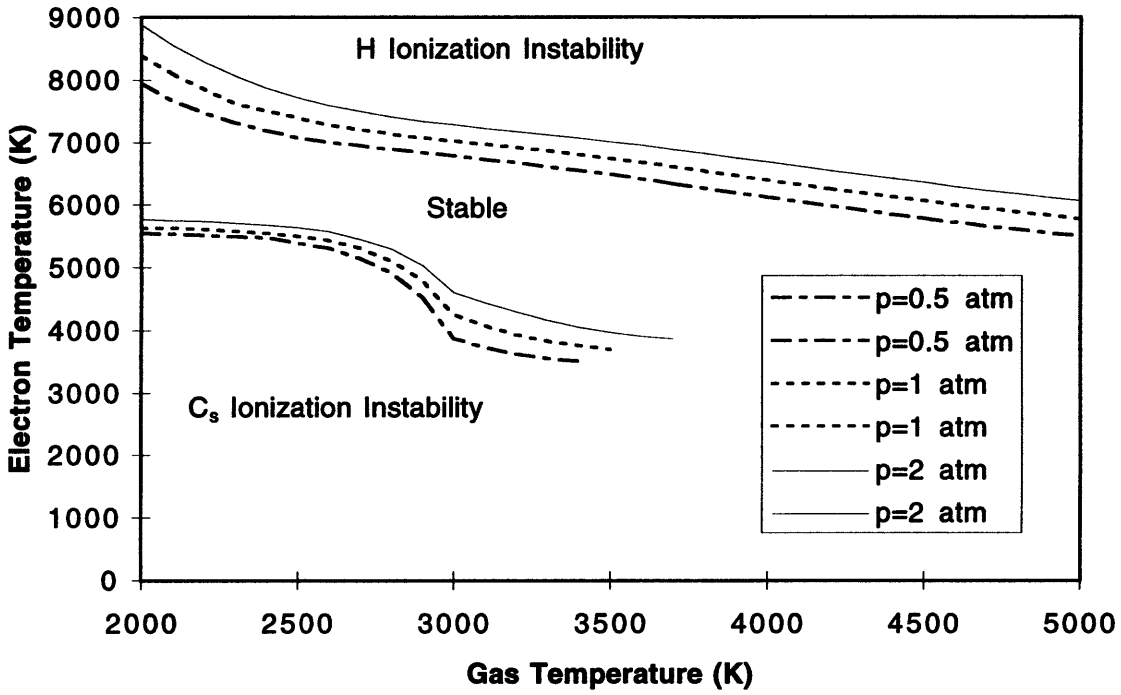

Figure 4-6: Threshold values of electron temperature versus gas temperature at different pressures

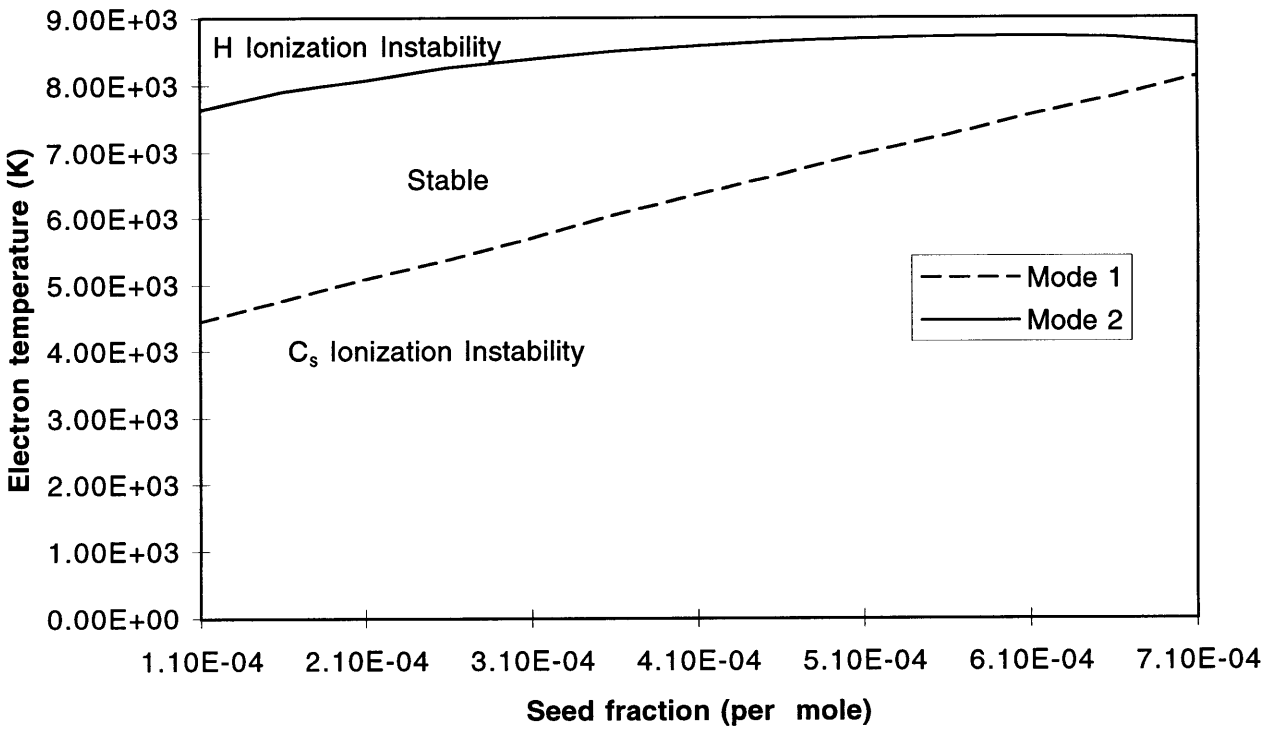

Figure 4-7: Threshold values of electron temperature versus cesium seed fraction

Chapter 5

Conclusions

5.1 Achievements

The feasibilty of alkali seeding as an approach toward reducing frozen losses in hydrogen arcjets has been theoretically investigated. Results based on a quasi one dimensional equilibrium steady model show that, with reasonable constraints on the constrictor geometry, without allowing the electron temperature to exceed $7000K$, and with cesium mass fraction as low as 2%, a specific impulse of about 850 second is attainable with no frozen losses. The constraint on electron temperature was imposed primarily to avoid ionization instabilities associated with the presence of hydrogen ions in the system. The occurrence of this instability could lead to a transition into conventional hydrogen arc or quenching of the arc. Hence, it is of utmost importance to probe the behavior of the system in this regime.

A small perturbation analysis was performed to address this concern. Results from this analysis suggest that there are actually two regimes in which ionization instabilites occur in the system. The first, the seed ionization instability, was found to occur in regions where the seed is not fully ionized, and where coulombic interactions are very important. It was also found to dissappear after the seed is fully ionized. As a result, It was concluded that its effect on the system would be to drive the electron temperature above its threshold values to near full ionization of the seed. The other mode of instability was found to occur at temperatures, where the dissociation and ionization of hydrogen are significant. The behavior of these two modes of instability on background parameters; pressure, temperatures (both T and T_e) and seed fraction, was explained. A critical seed fraction at which the system is always unstable was identified.

Based on the results from these analysis, it can be concluded that alkali seeding is indeed a viable approach to eliminating frozen losses in arcjets.

5.2 Recommendation for Future Work

Because of the preliminary nature of this work, certain issues in the flow physics were ignored for sake of simplicity. Foremost amongst these is the effect of viscosity. This is the reason why in the quasi one dimensional analysis, a restriction was imposed on the channel length. There is a need to also investigate effects of nozzle flow kinetics and radiation on the overall performance. Also neglected in the analyses were near electrode effects, especially around the cathode area, where a gaussian-like temperature distribution was assumed. Unfortunately, the physics of the electrodes is one of the least understood problems in arcjets, and is a subject of current research. Other concerns that also need to be addressed are plume and contamination issues, since cesium mass fraction of 2% may begin to approach the contamination levels due to electrode erosion. It would also be worthwhile to investigate other parent-seed configuration e.g. helium seeded with pottasium or cesium.

In view of this, it is recomended that more detailed theorectical design studies be pursued, and that plans be made for experimental work in this area.

Appendix A

Tables of Hydrogen Collision Cross Sections and Integrals

Table A.1: Average Electron Collision Cross-Sections

$Q_{ij}(10^{-20}m^2)$		
T_e	Q_{eH_2}	Q_{eH}
1000	10.1	31.18
2000	11.3	27.65
3000	12.6	26.01
4000	13.4	24.54
5000	14.2	23.20
6000	14.8	21.96
7000	15.5	20.83
8000	15.9	19.80
9000	16.4	18.86
10,000	16.9	17.99
11,000	17.3	17.18
12,000	17.6	16.44
13,000	17.8	15.76
14,000	18.0	15.11
15,000	18.2	14.52

Table A.2: Average Effective Collision Integrals

$\bar{\Omega}_{ij}^{(l,m)}(10^{-20}m^2)$					
T_g	$\bar{\Omega}_{H_2H_2}^{(2,2)}$	$\bar{\Omega}_{H_2H}^{(2,2)}$	$\bar{\Omega}_{HH}^{(2,2)}$	$\bar{\Omega}_{H_2H_2}^{(1,1)}$	$\bar{\Omega}_{HH}^{(1,1)}$
1000	6.00	5.13	5.95	5.21	5.24
1500	5.59	4.52	5.22	4.66	4.57
2000	5.33	4.10	4.74	4.37	4.13
2500	5.02	3.79	4.39	4.04	3.82
3000	4.73	3.55	4.12	3.79	3.57
3500	4.50	3.35	3.90	3.59	3.37
4000	4.29	3.18	3.74	3.42	3.23
4500	4.12	3.03	3.61	3.27	3.12
5000	3.97	2.91	3.50	3.14	3.03

References

[1] Bittencourt, J. A., "Fundamentals of Plasma Physics", Pergamon Press, 1986, New York.

[2] Brode, R. B., "The Qualitative Study of the Collisions of Electrons with Atoms", Rev. Mod. Phys., vol 5, no. 4, p. 257, 1933.

[3] Chapman, S. and Cowling, T. G., *The Mathematical Theory of Non-Uniform Gases*, Cambridge, 1953.

[4] Hirschfelder, J. O., Curtiss, C. F. and Bird, R. B., *Molecular Theory of Gases and Liquids*, John Wiley and Sons, Inc., New York, 1954.

[5] Jahn, R. G., "Physics of Electric Propulsion", McGraw-Hill Book company, 1968, New York.

[6] Janev, R. K., Langer, W. D., Evans, Jr., K. and Post ,Jr, D. E., *Elementary Processes in Hydrogen-Helium Plasmas*, Springer-Verlag, New York, 1987.

[7] Jack, J. R., "Theorectical Performance of Propellants Suitable for Electrothermal Jet Engines", ARS J., vol 31, p. 1685, 1961.

[8] Lee, T. H., *Physics and Engineering of High Power Switching Devices*, MIT Press, Cambridge, Massachussets, 1975.

[9] Martinez-Sanchez, M. and Sakamoto, A., "Simplified Analysis of Arcjet Thrusters", AIAA 93-1904. 29th Joint Propulsion Conference, Monterey, CA, June 1993.

[10] Miller, S. A., *Multifluid Nonequilibrium Simulation of Arcjet Thrusters*, Doctoral Thesis, Massachusetts Institute of Technology, 1994.

[11] Mitchner, M. and Kruger, C., *Partially Ionized Gases*, John Wiley and Sons, New York, 1973.

[12] Pfender, E., "Electric Arcs and Arc Gas Heaters", *Gaseous Electronics*, Volume 1. Academic Press, 1978.

[13] Rogers, C. R. and Schexnayder, C. J., "Chemical Kinetic Analysis of Hydrogen-Air Ignition and Reaction Times", NASA TP-1856, 1981.

[14] Rosa, R. J., *Magnetohydrodynamic Energy Conversion*, Hemisphere Publishing Corporation, 1987.

[15] Sheppard, E. J., *Ionization Nonequilibrium and Ignition in Plasma Accelerators*, Doctoral Thesis, Massachusetts Institute of Technology, 1994.

[16] Sutton, G. W. and Sherman, A., *Engineering Magnetohydrodynamics*, McGraw-Hill, New York, 1965.

[17] Wallner, L. E. and Czika, J.,Jr., Arc-jet Thrustor for Space Propulsion, *NASA Tech. Note D-2868, June, 1965.*